Int J Earth Sci (Geol Rundsch) (2015) 104:1061–1081
DOI 10.1007/s00531-014-1129-z

ORIGINAL PAPER

Late Miocene accelerated exhumation of the Daliang Mountains, southeastern margin of the Tibetan Plateau

Bin Deng · Shu-gen Liu · Eva Enkelmann · Zhi-wu Li · Todd A. Ehlers · Luba Jansa

Received: 16 July 2014 / Accepted: 11 December 2014 / Published online: 28 December 2014

Abstract The Late Cenozoic evolution of the southeastern margin of the Tibetan Plateau has been well documented, but controversies remain concerning Late Cenozoic acceleration of exhumation. We present 41 new apatite and zircon (U–Th)/He ages from six transects in the Daliang Mountains that provide constraints on the timing and the rate of denudation. We calculated exhumation rates for the transects based on the age versus elevation/structural depth relationship. The results are consistent across the Daliang Mountains and indicate a protracted period of slow cooling and denudation from ~30 to ~10 Ma, with an exhumation rate of ~0.15 mm/year. This slow exhumation is followed by accelerated rates of ~0.4–0.8 mm/year since ~10 Ma. The protracted slow denudation and long residence time within the apatite helium partial retention zone resulted in large variations in single-grain (U–Th)/He ages. We suggest that the post ~10-Ma rapid cooling and exhumation in the Daliang Mountains is driven by the eastward growth of the Tibetan Plateau. Furthermore, we suggest that the mountain building in the Daliang Mountains result from the crustal shortening accompanied with transpression, rather than from the lower crustal channel flow.

Keywords (U–Th)/He · Thermochronology · Denudation · Daliang Mountains · Southeastern margin of Tibetan Plateau

B. Deng (✉) · S. Liu · Z. Li
State Key Laboratory of Oil and Gas Reservoir Geology and Exploitation, Chengdu University of Technology, Chengdu 610059, China
e-mail: Dengbin3000@163.com

B. Deng · E. Enkelmann · T. A. Ehlers
Department of Geosciences, Universität Tübingen, 72074 Tübingen, Germany

E. Enkelmann
Department of Geology, University of Cincinnati, Cincinnati, OH, USA

L. Jansa
Geological Survey of Canada-Atlantic, Dartmouth, NS, Canada

Introduction

Progressive Indo-Eurasian convergence induces numerous lithospheric-scale strike-slip faults and orogenic thrusts, which partly account for the Tibetan Plateau formation and its margin construction during the Cenozoic (Tapponnier et al. 2001; Royden et al. 2008). Large-scale Tibetan crustal mass is currently moving eastwards and rotating clockwise around the eastern Himalayan syntaxis (Fig. 1). Most of the motion is redirected into northeast and southeast flow around the Sichuan Basin (Clark and Royden 2000; Zhang et al. 2004b; Enkelmann et al. 2006), due to the backstop from the craton-like lithosphere of the Sichuan Basin (Copley 2008; Liu et al. 2012). Although no significant shortening has been observed across the eastern and southeastern margin of the Tibetan Plateau by geodetic and geologic studies (Burchfiel et al. 1995; Wang et al. 1998; Zhang et al. 2004b; Shen et al. 2005), the margin has experienced extensive deformation and denudation during Cenozoic time due to the far-field effect of the Indo-Eurasia convergence. There is widespread thrusting within the Longmen Mountains, and strike-slip motion along the Xianshuihe fault, the Red River fault, and other large-scale strike-slip systems (Wang et al. 1998; Hubbard and Shaw 2009; Zhang et al. 2010), resulting in significantly different topography along the eastern margin of the Tibetan Plateau

(Kirby et al. 2002; Clark et al. 2005) (Fig. 1). Low-temperature thermochronology investigations have yielded valuable insights into the exhumation history of the eastern margin of the Tibetan Plateau (Fig. 1). Late Cenozoic cooling ages at the Songpan–Ganzi area reflect regional denudation of the eastern Tibetan Plateau. This regional denudation has been interpreted as a response to crustal thickening (Arne et al. 1997; Kirby et al. 2002; Li et al. 2012), lower crustal channel flow (Clark and Royden 2000; Mukherjee 2005; Godard et al. 2009a), and drainage reorganization (Richardson et al. 2008). Recently, Ouimet et al. (2010) inferred a relatively constant and uniform regional uplift at ~10 Ma in the southeastern margin of the Tibetan Plateau, by using zircon and apatite (U–Th)/He data. However, Wang et al. (2012a) argued that two phases of rapid exhumation took place at 30–25 and at 15–10 Ma ago, respectively. Most of the previous studies concentrated on the Songpan–Ganzi fold and thrust belt, but studies at further southeastern margins of the Tibetan Plateau are rare (Fig. 1).

The Daliang Mountains represent the boundary between the southeastern Tibetan Plateau and the Sichuan Basin (Fig. 1). This paper presents new apatite and zircon (U–Th)/He (AHe and ZHe, respectively) thermochronometry results from the Daliang Mountains, which indicate multiple periods of cooling and denudation during the Cenozoic transpressional strike-slip tectonics. The new data supports an interpretation that (1) cooling and exhumation with apparent rates of ~0.15 mm/year from ~30 to ~10 Ma were pervasive across the region and (2) Late Cenozoic eastward growth of the Tibetan Plateau controlled the rapid post ~10-Ma cooling and denudation in the Daliang Mountains. The results from the Daliang Mountains provide an example of how low-temperature thermochronometry can provide additional information on the denudation and mountain building at low-relief topographic regions, especially in absence of syn- to post-deformational strata.

Geological setting

The ~300-km-long and ~80-km-wide Daliang Mountains chain marks the southwestern boundary of the Sichuan Basin and of the southeastern margin of the Tibetan Plateau. The Daliang Mountains are located at the western margin of the Yangtze craton (South China Block) and are nearly N–S trending (Fig. 1). This mountain range is characterized by north–south-trending low- to medium-grade metamorphic rocks of Proterozoic and Archean age (Zhang et al. 1990; BGMRSP 1991; Luo 1998; Zheng et al. 2006), which comprise the basement of the Yangtze craton. The area underwent complicated tectonic evolution from a continental margin during Paleozoic–Mesozoic times to collisional orogeny since the Late Triassic and Cenozoic (Burchfiel et al. 1995; Chen et al. 2011). The Phanerozoic strata are dominated by Silurian–Triassic marine clastic–carbonate sequences, and Permian continental flood basalts that widely cover the western margin of the Yangtze craton (Xu et al. 2001; He et al. 2007). Post Late Triassic terrestrial sediments are dominated by fluvial and lacustrine red bed facies with only sparse outcrops of Cenozoic rocks. The terrestrial sediments are laterally synchronous and comparable between the Panzhihua–Xichang area and the Sichuan Basin. Moreover, the similarity and comparability in sediment, depositional facies, and paleontology indicate that both basins were linked as a paleo-Sichuan Basin during Mesozoic time (Xia 1982; Zhang et al. 1990; BGMRSP 1991; Guo et al. 1996).

Fig. 1 Map of the southeastern margin of the Tibetan Plateau and the Daliang Mountains. The locations of sample transects for this study are indicated by *blue stars* (vertical transects) and *black lines* (vertical vs. depth transects). Recent thermochronological data of age–elevation profiles are indicated in *yellow*, *white*, *purple*, *gray*, *deep gray*, *black stars*, and *red star* are from Liu et al. (2008); Richardson et al. (2008), Li et al. (2012); Clark et al. (2005), Ouimet et al. (2010), Godard et al. (2000b), and Wang et al. (2012a, b), respectively. The ~0.25 mm/year, ca. 9 Ma indicate that rapid exhumation with rate of ~0.25 mm/year began at ca. 9 Ma. *Inset* shows the location of eastern margin of Tibetan Plateau with the *box* that outlines the study area. The Indian plate motion vector with 36–40 mm/year showed by *black arrow* is after Zhang et al. (2004a, b); the *red arrows* show the eastward growth of Tibetan Plateau. EHS—eastern Himalayan syntaxis (the *red triangle*), XSH F.—Xianshuihe fault, DLS F.—Daliangshan fault, ANH F.—Anninghe fault, XJ F.—Xiaojiang fault, MPS F.—Mopanshan fault, JH F.—Jinghe fault, GS G.—Gonga shan granites. *a* Xide transect, *b* Mianshan transect, *c* Ganluo transect, *d* Wushihe transect, *e* Muchuan transect, *f* Wudu transect

The Daliang Mountains comprise a series of N to NNW sinistral strike-slip faults (e.g., Jinghe fault, Anninghe fault, Xiaojiang fault). Our field studies indicate that the Daliang Mountains are weakly deformed and the strata outcrop predominantly horizontally, or with a low inclination. There are two different phases that are generally controlling the tectonic framework of the eastern Tibetan Plateau after the Late Triassic. During the Late Triassic, the Songpan–Ganzi units, comprised by thick sequence of deep marine Triassic strata, often called the Songpan–Ganzi flysch (BGMRSP 1991), were thrust southeastward onto the Yangtze craton (Sichuan Basin), along the Longmen thrust belts, to form the western Sichuan foreland basin (Fig. 1; Chen et al. 1995; Worley and Wilson 1996; Deng et al. 2012a). The thrusting along the Jinghe fault farther south formed the Panzhihua–Xichang Basin (Fig. 1; BGMRSP 1991; Burchfiel et al. 1995). Thrusting with sinistral strike-slip occurred initially during the Late Triassic (Dirks et al. 1994; Chen et al. 1995; Worley and Wilson 1996), but was reactivated during Cenozoic time as a dextral strike-slip in the north and sinistral strike-slip in the south (Chen et al. 1994; Burchfiel et al. 1995; Wang and Burchfiel 2000).

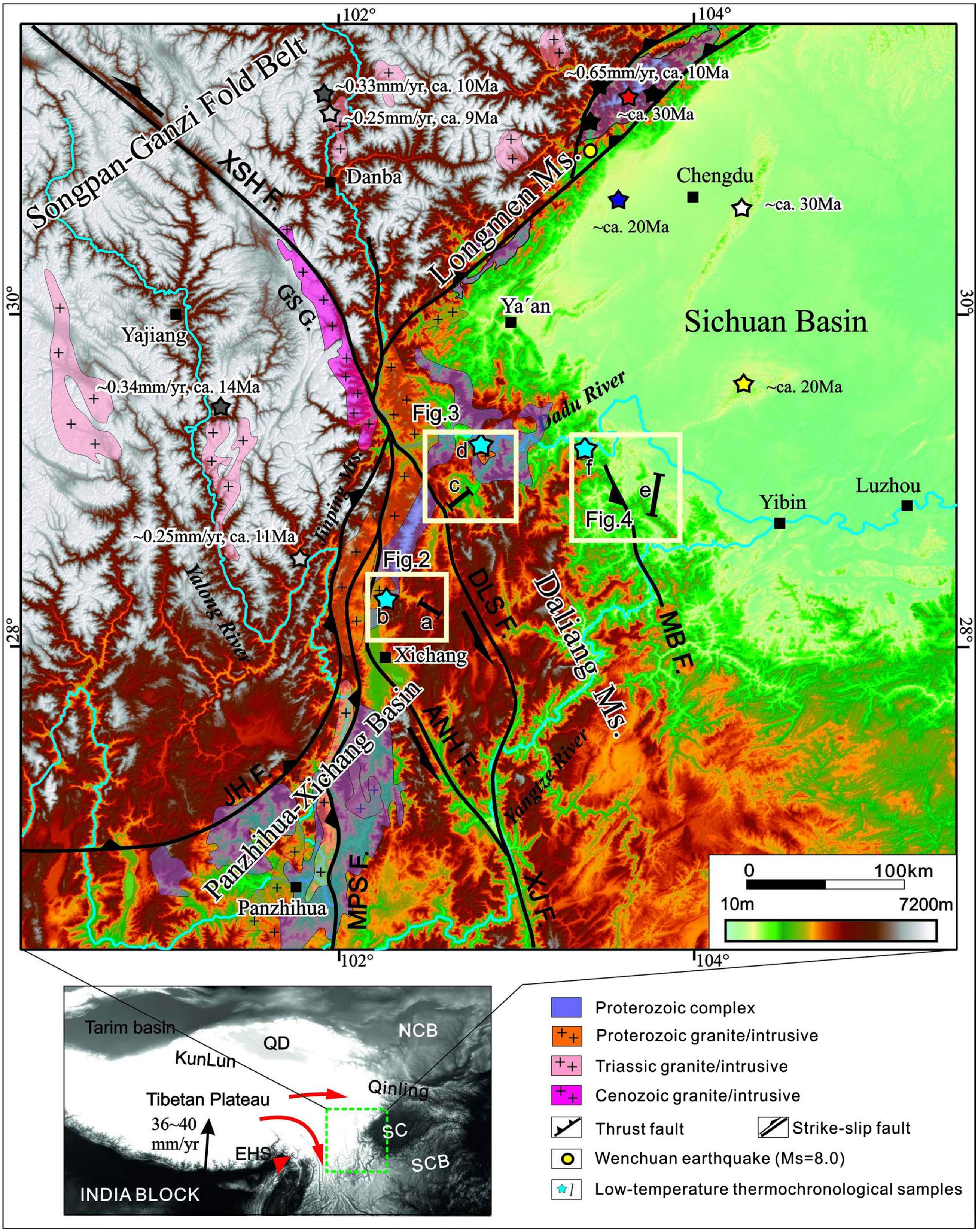

102°
104°
30°
28°
Songpan-Ganzi Fold Belt
XSH F.
~0.33mm/yr, ca. 10Ma
~0.25mm/yr, ca. 9Ma
~0.65mm/yr, ca. 10Ma
~ca. 30Ma
Danba
Longmen Ms.
Chengdu
~ca. 30Ma
~ca. 20Ma
GS G.
Yajiang
Ya´an
Sichuan Basin
~0.34mm/yr, ca. 14Ma
~ca. 20Ma
Dadu River
Fig.3
d
c
f
e
Fig.4
Yibin
Luzhou
Jinping Ms.
~0.25mm/yr, ca. 11Ma
Yalong River
Fig.2
b
a
Xichang
DLS F.
Daliang Ms.
MB F.
Panzhihua-Xichang Basin
ANH F.
JH F.
Yangtze River
MPS F.
XJ F.
Panzhihua
0
100km
10m
7200m
Tarim basin
QD
NCB
KunLun
Qinling
Tibetan Plateau
36~40 mm/yr
SC
EHS
SCB
INDIA BLOCK
Proterozoic complex
Proterozoic granite/intrusive
Triassic granite/intrusive
Cenozoic granite/intrusive
Thrust fault
Strike-slip fault
Wenchuan earthquake (Ms=8.0)
Low-temperature thermochronological samples

The reactivation of older structures has been interpreted as the result of the Late Cenozoic eastward or southeastward extrusion of crustal material from the Tibetan Plateau and subsequent clockwise rotation around the eastern Himalayan syntaxis (Wilson et al. 2006; Schoenbohm et al. 2006a; Royden et al. 2008). The Xianshuihe–Anninghe–Xiaojiang fault forms the natural southeastern boundary for the clockwise rotation (Wang et al. 1998; He et al. 2008). This fault marks a major strike-slip system, where the Panzhihua–Xichang area or even the southeastern margin of the Tibetan Plateau seems to be moving actively by sinistral strike-slip for more than ~60 km, relative to the western edge of the Sichuan Basin (Wang et al. 1998; Zhang et al. 2004b; Shen et al. 2005; Schoenbohm et al. 2006b). $^{40}Ar/^{39}Ar$, U–Pb and Rb–Sr data indicate that a rapid cooling event occurred along the Xianshuihe fault zone during 12–10 Ma, coevally with the emplacement and deformation of the Gonga Shan granite (Roger et al. 1995; Zhang et al. 2004a). The Gonga Shan region accommodates extensive uplift and denudation at the southeastern margin of the Tibetan Plateau during this time (Xu and Kamp 2000; Lai et al. 2007; Clark et al. 2005; Ouimet et al. 2009, 2010).

Sample transects and methods

In the Daliang Mountains, samples were collected on three transects along one limb of an anticline, with wavelengths more than 20 km (e.g., Xide, Ganluo, Muchuan). The isotherms represented by helium age were probably perturbed by the deformation. Samples comprise Late Triassic to Early Cretaceous strata within a ~2-km-long stratigraphic profile (Table 1; Figs. 2, 3, 4). The other samples were collected from 3–1.1 km vertical transects in Precambrian granites (e.g., Mianshan granite, Wudu granite, Wushihe granite), over a short horizontal distance of ~4–9 km (Fig. 5). All the anticlines that were sampled are characterized by gentle-to-moderate deformation, whereas the granites are undeformed and lack significant foliation and/or lineation.

The Muchuan and Wudu transects are located at the southeastern margin of the Daliang Mountains at elevations between 400 and 1,200 m (Fig. 4). The Ganluo and Wushihe transects are located within the Daliang Mountains at elevations between 600 and 1,300 m (Fig. 3), and the Xide and Mianshan transects are at the western margin of the Daliang Mountains at elevations between 1,700 and 3,000 m (Fig. 2).

Based on detailed orientations of the stratigraphy in the structural profiles, we can construct a stratigraphic column (Figs. 2, 3, 4). Because no faults are present and insignificant thickness variations are observed within each section, we argue that the error in estimated stratigraphic thickness and sample location is less than ~100–200 m and that the restored stratigraphic column from a single anticlinal structure can be used as a proxy for original depth. Thus, a plot of stratigraphic depth (structural depth) versus sample age can be constructed to calculate the exhumation rate over time. The other three transects in granites can be used for a comparison, using an age versus elevation relationship. All exhumation rates were derived by the linear regression of the structural depth/elevation versus ages using Isoplot (Ludwig 2003).

We used apatite and zircon (U–Th)/He thermochronometry on minerals separated from sedimentary and granitic rocks in order to gain information about the cooling history of these rocks. For an effective grain radius of ~60 μm and a cooling rate of ~10 °C/Myear, the closure temperatures of the (U–Th)/He system in apatite and zircon are ~65 °C (Wolf et al. 1998; Farley 2000), and ~180 °C (Reiners et al. 2004), with their relative helium partial retention zone (HePRZ) of ~50–80 and ~160–200 °C (Wolf et al. 1998; Stockli 2005), respectively.

Apatite and zircon grains were separated from rocks by crushing, sieving, and washing the samples, and using standard magnetic and heavy liquid separation techniques. Clear and undisturbed apatite and zircon grains without inclusions were selected using a binocular microscope. The grain dimensions were measured for the calculation of the alpha correction factor after Farley et al. (1996). Afterward individual grains (usually three replicates per sample, and each replicate was a single grain) were, respectively, packed in Nb-tubes for (U–Th)/He analysis. The helium gas was first extracted in the Patterson helium extraction line equipped with a 960-nm diode laser at the University of Tübingen. Each sample was reheated at the same conditions to ensure that all helium was extracted. The re-extracted component of helium gas showed typically <1 % of the first signal. After Helium analysis, the grain packages were sent to the University of Arizona at Tucson for U, Th, and Sm measurements using an ICP-MS. The analytical errors of the mass spectrometer measurements are generally very low and do not exceed 2 %. In contrast, the alpha correction factor and reproducibility of the sample age constitute a much larger error. We therefore report the mean (U–Th)/He age and the standard deviation of the measured aliquots as the sample error (1σ).

Results

Fifty-nine AHe ages (18 AHe samples), ranging from 4 to 50 Ma, and 63 ZHe ages (22 ZHe samples), ranging from 5 to 230 Ma, were measured (Table 1). Thirteen samples are Upper Triassic to Upper Jurassic sandstones, and twenty samples are Precambrian granites. A summary of

Table 1 Apatite and zircon (U–Th)/He results

Transect	Lon/Lat (°N/°E)	Elev. (m)	Rock type	Sample ID	4-He (mol)	238-U (mol)	232-Th (mol)	147-Sm (mol)	[eU] (ppm)	Raw age (Ma)	Error ± 1σ (Ma)	Ft	Corrected age (Ma)	Error ± 2σ (Ma)	Mean age ± 1 error (Ma)
Xide	28.2646	1909	Sandstone	SYX01_1a	3.56E−15	1.73E−13	1.34E−12	2.58E−13	293	5.74	0.3	0.600	9.56	0.5	
	102.4768		T_3–J_1b	SYX01_2a	4.20E−15	1.59E−13	1.87E−12	3.61E−13	265	5.56	0.3	0.632	8.79	0.4	9.18 ± 0.5
				SYX01_1z	3.50E−14	1.18E−12	9.09E−13			19.53	0.9	0.688	28.37	1.4	
				SYX01_2z	2.44E−14	8.60E−13	9.01E−13			17.71	0.9	0.683	25.91	1.3	
				SYX01_3z	8.50E−14	4.58E−12	1.88E−12			13.14	0.7	0.671	19.56	1.0	24.6 ± 4.5
	28.2648	1952	Sandstone	SYX03_1z	2.20E−13	6.79E−12	4.02E−12			22.06	1.1	0.724	30.45	1.5	
	102.5032		J_2n	SYX03_2z	4.81E−13	1.38E−11	2.01E−12			25.98	1.3	0.779	33.32	1.7	
				SYX03_3z	3.46E−13	6.91E−12	1.85E−12			36.41	1.8	0.737	49.34	2.5	37.7 ± 10
	28.2164	2032	Sandstone	SYX06_1a	1.48E−15	2.51E−13	5.43E−13	4.00E−13	95	3.05	0.2	0.719	4.24	0.2	
	102.535		J_3f	SYX06_3a	8.94E−16	5.92E−14	1.14E−13	7.68E−13	40	7.77	0.4	0.649	11.97	0.6	
				SYX06_4a	1.24E−15	1.26E−13	4.97E−13	3.74E−13	101	3.99	0.2	0.656	6.08	0.3	7.43 ± 4
Muchuan	28.9032	476	Sandstone	SQM07_1a	7.67E−15	3.13E−13	1.19E−13	3.64E−13	136	17.35	0.9	0.677	25.60	1.3	
	103.8825		J_2s	SQM07_2a	1.61E−15	3.80E−14	3.17E−13	8.84E−13	25	10.89	0.5	0.708	15.38	0.8	
				SQM07_3a	9.44E−16	1.82E−14	7.99E−14	2.85E−13	12	19.29	1.0	0.670	28.78	1.4	
				SQM07_4a	2.26E−15	7.52E−14	3.95E−13	1.02E−12	56	10.28	0.5	0.673	15.27	0.8	
				SQM07_5a	5.77E−16	1.25E−14	7.59E−14	1.75E−13	16	14.57	0.7	0.613	23.76	1.2	21.8 ± 6.1
	28.8934	494	Sandstone	SQM08_1a	4.20E−15	7.44E−14	5.19E−13	4.26E−13	35	16.71	0.8	0.728	22.95	1.1	
	103.8778		J_2z	SQM08_2a	3.24E−15	1.46E−13	5.76E−13	4.93E−13	62	8.95	0.4	0.724	12.36	0.6	
				SQM08_3a	1.14E−14	4.84E−13	1.21E−12	6.37E−13	128	11.55	0.6	0.748	15.44	0.8	
				SQM08_4a	4.21E−15	2.32E−13	5.05E−13	7.03E−13	74	9.29	0.5	0.734	12.66	0.6	15.9 ± 4.9
				SQM8-1z	3.60E−13	1.67E−11	4.98E−12			15.59	0.8	0.738	21.11	1.1	
				SQM8-2z	1.70E−12	7.27E−12	1.38E−12			170.90	8.5	0.746	227.89	11.4	
				SQM8-3z	2.18E−12	1.20E−11	3.73E−12			130.20	6.5	0.753	172.25	8.6	not reset
	28.8867	569	Sandstone	SQM11_1a	4.80E−16	1.86E−14	7.14E−14	1.49E−13	34	10.43	0.5	0.538	19.38	1.0	
	103.8724		J_2sn	SQM11_2a	3.72E−15	1.23E−13	5.34E−14	1.76E−13	183	21.17	1.1	0.520	40.65	2.0	
				SQM11_3a	1.98E−15	7.31E−14	4.39E−13	2.53E−13	279	8.81	0.4	0.455	19.35	1.0	26.5 ± 12
	29.008	360	Sandstone	SQM05_1a	1.05E−15	2.95E−14	9.17E−14	2.53E−13	24	15.69	0.8	0.644	24.36	1.2	
	103.8943		K_1	SQM05_2a	2.83E−14	4.07E−13	9.57E−13	8.88E−13	208	34.76	1.7	0.692	50.17	2.5	
				SQM05_3a	2.28E−16	9.25E−15	6.15E−14	3.37E−14	8	7.53	0.4	0.663	11.35	0.6	par.reset
	28.8973	583	Sandstone	SQM10_01a	2.90E−15	2.58E−13	1.32E−12	7.03E−13	123	3.99	0.2	0.718	5.56	0.3	
	103.8962		T_3–J_1x	SQM10_02a	3.83E−15	1.90E−13	1.55E−12	1.93E−13	149	5.45	0.3	0.691	7.89	0.4	
				SQM10_03a	3.53E−14	9.16E−13	6.07E−12	8.45E−13	408	11.87	0.6	0.737	16.11	0.8	9.85 ± 5.5
				SQM10-1z	2.14E−12	1.27E−11	6.10E−12			116.36	5.8	0.743	156.06	7.8	
				SQM10-2z	6.15E−13	2.98E−12	2.44E−12			133.22	6.7	0.744	178.38	8.9	
				SQM10-3z	2.07E−12	1.36E−11	7.84E−12			103.08	5.2	0.779	132.00	6.6	not reset

Table 1 continued

Transect	Lon/Lat (°N/°E)	Elev. (m)	Rock type	Sample ID	4-He (mol)	238-U (mol)	232-Th (mol)	147-Sm (mol)	[eU] (ppm)	Raw age (Ma)	Error ± 1σ (Ma)	Ft	Corrected age (Ma)	Error ± 2σ (Ma)	Mean age ± 1 error (Ma)
Ganluo	28.9639	1064	Sandstone	SS22_1a	1.38E−14	7.63E−13	2.33E−12	1.61E−12	133	8.21	0.4	0.786	10.44	0.5	
	102.7263		J_2x	SS22_2a	8.89E−16	9.56E−14	4.75E−13	5.16E−13	51	3.34	0.2	0.699	4.77	0.2	
				SS22_3a	8.23E−15	8.40E−13	1.30E−12	6.69E−13	493	5.59	0.3	0.664	8.42	0.4	7.88 ± 2.9
	28.9479	1352	Sandstone	SS24_1a	1.06E−14	7.21E−14	2.96E−13	7.06E−13	44	56.97	2.8	0.689	82.5	4.1	
	102.714		J_2y	SS24_2a	3.07E−15	4.98E−14	1.41E−13	1.38E−13	106	28.70	1.4	0.496	57.7	2.8	
				SS24_3a	2.24E−15	2.17E−13	6.68E−13	4.92E−13	311	4.66	0.2	0.574	8.12	0.4	
				SS24_4a	5.83E−15	4.02E−14	1.72E−13	3.88E−13	30	55.39	2.8	0.660	83.7	4.2	par.reset
	28.9301	1376	Sandstone	SS26_1a	7.01E−15	8.24E−13	1.28E−12	1.84E−12	314	4.82	0.2	0.712	6.77	0.3	
	102.7146		T_3–J_1b	SS26_2a	6.94E−15	5.84E−13	1.57E−12	5.38E−13	357	5.70	0.3	0.674	8.45	0.4	
				SS26_3a	5.94E−15	4.40E−13	2.40E−12	8.87E−13	395	4.64	0.2	0.658	7.05	0.4	
				SS26_4a	1.41E−15	1.51E−14	1.66E−12	3.11E−13	180	2.77	0.1	0.606	4.58	0.2	6.71 ± 1.6
				SS26_1z	2.20E−13	6.15E−12	2.48E−12			25.37	1.3	0.720	35.21	1.8	
	28.9452	1360	Sandstone	SS25_1a	1.66E−15	9.09E−14	8.13E−13	4.07E−13	95	4.63	0.2	0.668	6.93	0.3	
	102.7132		T_3–J_1b	SS25_2a	5.08E−16	9.17E−14	6.97E−14	2.18E−13	76	3.62	0.2	0.611	5.92	0.3	
				SS25_3a	1.57E−15	1.04E−13	1.62E−13	4.04E−13	28	8.49	0.4	0.637	13.32	0.7	
				SS25_4a	2.69E−16	4.85E−14	4.17E−14	1.39E−13	31	3.54	0.2	0.641	5.53	0.3	7.92 ± 3.6
	28.9501	1323	Sandstone	SS23_1a	6.79E−15	1.10E−13	1.19E−12	3.30E−13	150	13.74	0.7	0.651	21.10	1.1	
	102.7187		J_2y	SS23_2a	2.48E−15	1.81E−13	1.11E−12	2.53E−13	166	4.40	0.2	0.659	6.68	0.3	
				SS23_3a	1.18E−15	4.91E−14	8.68E−13	1.26E−13	204	3.68	0.2	0.544	6.77	0.3	11.5 ± 8.3
Mianshan	28.3052	2186	Granite	SYX18_1a	9.16E−15	5.41E−13	1.01E−12	3.70E−12	106	8.97	0.4	0.766	11.71	0.6	
	102.2814		P*t*	SYX18_2a	2.05E−15	1.36E−13	2.92E−13	1.69E−12	82	7.53	0.4	0.649	11.61	0.6	
				SYX18_3a	1.80E−15	1.19E−13	6.84E−13	6.75E−13	155	5.01	0.3	0.614	8.16	0.4	
				SYX18_4a	9.53E−16	1.08E−13	1.77E−13	7.15E−13	143	4.87	0.2	0.564	8.64	0.4	10.0 ± 1.9
				SYX18_1z	2.62E−13	1.91E−11	4.21E−12			10.08	0.5	0.758	13.29	0.7	
				SYX18_2z	3.05E−13	2.65E−11	7.58E−12			8.36	0.4	0.764	10.94	0.5	
				SYX18_3z	4.31E−13	2.81E−11	4.57E−12			11.42	0.6	0.756	15.10	0.8	13.1 ± 2.1
	28.3052	*2356*	*Granite*	SYX17_1z	6.79E−13	3.72E−11	1.92E−11			12.63	0.6	0.790	15.98	0.8	
	102.2845		*Pt*	SYX17_2z	3.59E−13	1.88E−11	8.89E−12			13.37	0.7	0.784	17.04	0.9	
				SYX17_3z	4.82E−13	2.51E−11	1.01E−11			13.62	0.7	0.804	16.93	0.8	16.7 ± 0.6
	28.3054	2685	Granite	SYX16_1a	5.60E−14	1.03E−12	7.24E−12	3.20E−12	448	16.11	0.8	0.741	21.73	1.1	
	102.2911		P*t*	SYX16_2a	1.56E−14	3.08E−13	4.33E−12	1.77E−12	376	9.26	0.5	0.667	13.88	0.7	
				SYX16_3a	2.10E−14	2.20E−13	1.31E−12	1.44E−12	134	30.97	1.5	0.700	44.21	2.2	par. reset
				SYX16-1z	2.20E−13	8.73E−12	1.64E−11			13.63	0.7	0.700	19.46	1.0	
				SYX16-2z	2.16E−13	6.57E−12	5.27E−12			21.48	1.1	0.732	29.32	1.5	
				SYX16-3z	1.71E−13	7.22E−12	8.53E−12			14.44	0.7	0.695	20.76	1.0	23.2 ± 5.4
	28.3056	*2749*	*Granite*	SYX14_1z	6.66E−13	7.52E−11	2.67E−11			6.34	0.3	0.744	8.52	0.4	
	102.2921		*Pt*	SYX14_2z	4.83E−13	6.01E−11	1.78E−11			5.83	0.3	0.716	8.14	0.4	
				SYX14_3z	8.75E−13	9.31E−11	3.99E−11			6.62	0.3	0.747	8.86	0.4	8.5 ± 0.4

Table 1 continued

Transect	Lon/Lat (°N/°E)	Elev. (m)	Rock type	Sample ID	4-He (mol)	238-U (mol)	232-Th (mol)	147-Sm (mol)	[eU] (ppm)	Raw age (Ma)	Error ± 1σ (Ma)	Ft	Corrected age (Ma)	Error ± 2σ (Ma)	Mean age ± 1 error (Ma)
	28.3062	2833	Granite	SYX13_1a	5.47E−15	1.69E−13	6.61E−13	1.60E−12	11	12.92	0.6	0.676	19.11	1.0	
	102.2933		P*t*	SYX13_2a	7.23E−15	1.21E−13	3.90E−13	1.42E−12	71	25.77	1.3	0.684	37.65	1.9	
				SYX13_3a	1.81E−15	4.18E−14	2.35E−13	5.88E−13	70	14.23	0.7	0.516	27.56	1.4	par.reset
	28.3068	*2904*	*Granite*	SYX12_1z	9.00E−13	2.23E−11	9.72E−11			15.66	0.8	0.781	20.05	1.0	
	102.2944		*Pt*	SYX12_2z	7.16E−13	3.96E−11	7.40E−11			9.82	0.5	0.788	12.46	0.6	
				SYX12_3z	4.92E−13	2.31E−11	3.04E−11			12.70	0.6	0.754	16.84	0.8	16.4 ± 3.8
	28.2964	1673	Granite	SYX11_1a	6.22E−15	2.66E−13	4.73E−13	3.04E−12	80	12.37	0.6	0.721	17.15	0.9	
	102.2284		P*t*	SYX11_2a	1.62E−15	1.96E−13	2.73E−13	1.35E−12	181	4.72	0.2	0.605	7.81	0.4	
				SYX11_3a	9.33E−15	2.66E−13	3.50E−13	2.20E−12	145	20.18	1.0	0.671	30.06	1.5	
				SYX11_4a	1.20E−15	2.02E−13	2.12E−13	1.77E−12	105	3.59	0.2	0.669	5.36	0.3	
				SYX11_1z	2.76E−13	2.66E−11	3.53E−12			7.81	0.4	0.747	10.45	0.5	
				SYX11_2z	2.26E−13	1.42E−11	2.24E−11			9.08	0.5	0.775	11.72	0.6	
				SYX11_3z	2.11E−13	1.79E−11	4.40E−12			8.61	0.4	0.763	11.28	0.6	11.1 ± 0.6
	28.3292	1793	Granite	SYX08_1a	2.70E−15	1.55E−13	2.74E−13	1.36E−12	85	9.34	0.4	0.665	14.04	0.7	
	102.348		P*t*	SYX08_2a	1.76E−15	1.82E−13	6.73E−14	5.57E−13	155	6.81	0.3	0.601	11.33	0.6	
				SYX08_3a	5.18E−15	4.00E−13	2.94E−13	2.03E−12	122	8.41	0.4	0.714	11.77	0.6	12.4 ± 1.5
Wushihe	29.3007	565	Granite	SS12_1a	6.48E−16	1.64E−14	1.14E−13	1.52E−13	26	11.64	0.6	0.595	19.56	1.0	
	103.1243		P*t*	SS12_2a	4.88E−16	1.59E−14	7.35E−14	1.08E−13	34	11.38	0.6	0.516	22.05	1.1	
				SS12_3a	4.52E−16	2.56E−14	1.20E−13	1.56E−13	45	6.50	0.3	0.552	11.78	0.6	
				SS12_4a	4.15E−16	3.20E−14	1.56E−13	1.84E−13	75	4.69	0.2	0.502	9.34	0.5	15.7 ± 6.1
	29.2363	1053	Granite	SS21_1z	7.973E−14	1.23E−11	1.38E−11			4.00	0.2	0.694	5.77	0.3	
	102.8402		Pt	SS21_2z	1.099E−12	5.39E−12	5.95E−12			124.78	6.2	0.645	192	9.6	
				SS21_3z	6.837E−13	6.36E−11	4.22E−11			7.22	0.4	0.695	10.39	0.5	8.1 ± 3.3
	29.2309	1402	Granite	SS19_1z	1.370E−13	1.21E−11	6.28E−12			7.82	0.4	0.739	10.58	0.5	
	102.8456		Pt	SS19_2z	1.011E−13	1.64E−11	1.63E−11			3.89	0.2	0.766	5.08	0.3	
				SS19_3z	4.528E−13	3.86E−11	1.84E−11			8.18	0.4	0.751	10.89	0.5	8.9 ± 3.3
	29.1981	715	Granite	SS15_1z	8.361E−13	1.17E−11	9.20E−12			46.62	2.3	0.727	64.03	3.2	
	102.8405		Pt	SS15_2z	2.862E−13	2.26E−11	1.88E−11			8.24	0.4	0.754	10.93	0.5	
				SS15_3z	4.695E−14	1.53E−11	1.52E−11			1.94	0.1	0.707	2.74	0.1	
	29.2333	1139	Granite	SS20_1z	3.818E−14	8.77E−11	8.13E−11			0.28	0.0	0.794	0.35	0.0	
	102.8404			SS20_2z	2.127E−13	3.17E−11	2.97E−11			4.28	0.2	0.743	5.76	0.3	
				SS20_3z	8.396E−14	3.03E−11	1.29E−11			1.96	0.1	0.752	2.60	0.1	2.9 ± 2.7
	29.2274	867	Granite	SS17_1z	9.315E−13	3.14E−11	1.80E−11			20.26	1.0	0.725	27.93	1.4	
	102.8363			SS17_2	1.852E−11	1.44E−11	1.68E−11			743.56	37.2	0.699	1039	51.9	
	29.2078	850	Granite	SS16_1z	9.458E−12	6.89E−12	3.78E−12			875.34	43.8	0.646	1304	65.2	
	102.844			SS16_2z	4.598E−12	1.56E−11	1.24E−11			190.47	9.5	0.688	275	13.8	
				SS16_3z	1.062E−11	1.83E−11	8.31E−12			392.28	19.6	0.699	553	27.7	

Table 1 continued

Transect	Lon/Lat (°N/°E)	Elev. (m)	Rock type	Sample ID	4-He (mol)	238-U (mol)	232-Th (mol)	147-Sm (mol)	[eU] (ppm)	Raw age (Ma)	Error ± 1σ (Ma)	Ft	Corrected age (Ma)	Error ± 2σ (Ma)	Mean age ± 1 error (Ma)
Wudu	29.2613	1265	Granite	SS04-1z	5.17E−13	2.52E−11	6.21E−12			15.04	0.8	0.764	19.67	1.0	
	103.4595			SS04-2z	6.14E−13	3.70E−11	8.10E−12			12.22	0.6	0.793	15.41	0.8	
				SS04-3z	1.60E−12	2.35E−11	5.77E−12			49.68	2.5	0.765	64.85	3.2	par.reset
	29.2596	1166	Granite	SS02-1z	2.09E−13	1.54E−11	6.38E−12			9.59	0.5	0.702	13.66	0.7	
	103.4554			SS02-2z	3.73E−13	1.48E−11	2.67E−11			13.82	0.7	0.732	18.87	0.9	
				SS02-3z	5.59E−13	3.24E−11	3.40E−11			10.76	0.5	0.718	14.97	0.7	15.8 ± 2.7
	29.2912	482	Granite	SS01-1z	2.32E−13	1.17E−11	4.46E−12			14.07	0.7	0.703	20.00	1.0	
	103.4872			SS01-2z	7.84E−14	4.68E−12	1.12E−12			12.28	0.6	0.688	17.84	0.9	
				SS01-3z	2.29E−13	7.20E−12	3.61E−12			22.07	1.1	0.716	30.80	1.5	22.9 ± 6.9
	29.2627	791	Granite	SS09-1z	3.77E−13	1.88E−11	8.48E−12			14.03	0.7	0.773	18.15	0.9	
	103.4774			SS09-2z	3.63E−13	1.09E−11	3.64E−12			24.00	1.2	0.765	31.35	1.6	
				SS09-3z	7.78E−13	2.57E−11	6.04E−12			22.18	1.1	0.783	28.32	1.4	25.9 ± 6.9
	29.263	1033	Granite	SS6_1z	9.174E−12	3.85E−11	1.26E−11			169.19	8.5	0.721	233	11.7	
	103.4642			SS6_2z	6.097E−12	1.21E−11	3.14E−12			357.15	17.9	0.729	484	24.2	
				SS06-3z	6.30E−13	4.47E−12	1.70E−12			99.42	4.9	0.735	135	6.8	

Corrected Age is corrected for alpha ejection after Farley et al. (1996). Ft: alpha correction factor

eU: Effective U concentrations are computed as U + (0.235*Th) (Flowers et al. 2007). The U and Th concentrations in ppm were estimated by assuming a 3.2 g/cm3 apatite density, cylinder-shaped grain geometry, and using the measured grain dimensions. There is no a correlation between U concentration and AHe ages to rule out radiation damage trapping in our sample ages (Shuster et al. 2006; Flowers et al. 2007) all single-grain ages and mean ages is presented in Table 1. In most cases, apatite and zircon single-grain ages are substantially younger than depositional ages of the host rocks (or crystallization age of granite), and apatite ages are systematically younger than zircon ages from the same rock sample, or from the same stratigraphic column. ZHe ages of sediment samples with single-grain ages older than the depositional age are unreset, or partially reset (as apparent or mixed age) in the cases where some single-grain ages are younger and some are older than the deposition age.

Xide transect

Three samples were analyzed from the Xide transect located at the southeastern limb of Lianghekou anticline (Fig. 2; Table 1). The five AHe and six ZHe ages range from 4.2 ± 0.2 to 11.9 ± 0.7 Ma and from 19.6 ± 1.3 to 49.3 ± 4.0 Ma, respectively. The anticline is characterized by NE striking terrestrial sequences of the Baiguowan Formation that is Late Triassic to Early Jurassic in age (T_3–J_1b), and by the Upper Cretaceous Leidashu Formation (K_2l).

AHe ages of sample SYX06 from the top of the stratigraphic column range from 4.2 ± 0.2 to 11.9 ± 0.7 Ma with a mean age of 7.4 ± 4 Ma. The sample SYX01 from the base of the column yielded a similar age with mean AHe age of 9.2 ± 0.5 Ma (Table 1). The ZHe ages in the same section show a distinct decrease with increasing depth with mean ages of 37.7 ± 10 Ma (SYX03) and 24.6 ± 4.5 Ma (SYX01; Fig. 2). It should be noted that there is a different trend in AHe and ZHe age with increasing depth, which could be correlated with a large variation in single-grain AHe ages in SYX06, or the topography influence of the AHe system that is of lower closure temperature than in ZHe system.

All cooling ages are significantly younger than the depositional age of the host rock, indicating that these samples had been exposed to temperatures >180 °C after deposition. Using the different closure temperatures and the ages of the AHe and ZHe system for our samples, we can calculate the different exhumation rates for various time intervals (Reiners et al. 2003; Reiners and Brandon 2006). The difference between mean AHe and ZHe ages for the sample SYX01 is ~16 Ma and yields an exhumation rate of ~0.21 mm/year from ca. 24.6 ± 4.5 to 9.2 ± 0.5 Ma, assuming a paleo-geothermal gradient of ~30 °C/km (Hu et al. 2000) and a surface temperature of 10 °C.

Ganluo transect

At the Ganluo transect, five samples were collected from the Late Triassic to Early Jurassic Baiguowan Formation (T_3–J_1b) to Upper Jurassic Xincun Formation (J_2x) at the northeastern limb of the Yutian anticline (Fig. 3; Table 1). These samples provide thirteen AHe ages ranging from 4.6 ± 0.2 to 21.1 ± 3.1 Ma and only one ZHe age of 35.2 ± 3.4 Ma (Table 1). The NW striking anticline expose a sequence from the Emeishan basalt ($P_2\hat{a}$) to the Niuguntang Formation (J_2n). The undeformed Neogene Xigeda Formation outcrops horizontally and overlies the gentle Yutian anticline, indicating that the deformation occurred between Early Cretaceous and Late Cenozoic time.

AHe ages from the sample at the top of the stratigraphic column (SS22) yielded a mean age of 7.9 ± 2.9 Ma, and the sample SS26 from the base yielded a mean AHe age of 6.7 ± 1.6 Ma (Table 1). Overall, these AHe data from the Ganluo transect indicate an apparent exhumation rate of $0.8^{+INF}/_{-0.57}$ mm/year between ~9 and 5 Ma (Figs. 3, 6).

Furthermore, at the bottom of this transect, there is only one ZHe age of 35.2 ± 3.4 Ma from sample SS26. With only one replicate, it is difficult to be certain that the base of this transect is fully reset. Given that the ZHe age of the sample SS26 is substantially younger than the depositional age of the host rock (~175–220 Ma), we argue that the base of this transect is fully reset. Thus, the interval time of sample SS26 through the AHe and ZHe closure temperatures is ~29 Ma, suggesting an exhumation rate of ~0.13 mm/year from 35.2 ± 3.4 to 6.7 ± 1.6 Ma.

Muchuan transect

The Muchuan anticline transect is comprised by marine Permian to middle Triassic strata (P_1–T_2) and terrestrial Late Triassic to Early Jurassic (Xiangxi Group T_3–J_1x) to Lower Cretaceous strata. Five samples were collected at the northeastern limb of the Muchuan anticline (Fig. 4; Table 1), which provided 18 AHe ages, ranging from 5.6 ± 0.7 to 50.2 ± 3.1 Ma.

Single-grain AHe ages from the top of the stratigraphic column (SQM05) show a significant range from 11.4 ± 0.9 to 50.2 ± 3.1 Ma and are interpreted to represent an exhumed AHe PRZ (Table 1; Figs. 4, 6). The samples that are stratigraphically lower show a systematic decrease in the spread of the single-grain ages and also a decrease of the mean AHe ages with increasing structural depth (Fig. 4). The mean AHe ages decrease from 26.4 ± 12 Ma to a mean age of 9.9 ± 5.5 Ma at the base of the section. The linear regression indicates an apparent exhumation rate of $0.13^{+0.04}/_{-0.09}$ mm/year from ~30 to 9 Ma (Fig. 6).

Two samples in the lower part of the column yielded ZHe ages. At the base, the ZHe ages range from 132.0 ± 16.4 to 178.4 ± 20.1 Ma (Table 1), slightly younger than the depositional age. In contrast, the ZHe ages from sample SQM08 range from 21.1 ± 2.0 to 227.9 ± 16.7 Ma, with the two older ZHe ages predating deposition (Fig. 4). Excluding the 21.1 ± 2.0 Ma ZHe age that is unusually young, the ZHe ages within this transect display an increase in temperature with depth and reveal that none of these rocks had been exposed to temperatures >160–200 °C, high enough to reset zircon (U–Th)/He ages after deposition.

Mianshan transect

Eight samples within the Mianshan transect were collected from Precambrian granites (Fig. 5a). The ZHe ages in the Mianshan granite range from 8.1 ± 1.0 to 29.3 ± 2.8 Ma, with mean ages from 8.5 ± 0.4 to 23.2 ± 5.4 Ma (Table 1). The linear regression of the age–elevation plot shows an apparent exhumation rate of $0.15^{+INF}/_{-0.12}$ mm/year between ~20 and 10 Ma (Fig. 7b). Due to the sample SYX14 far off the regression line, it is occurred a low probability of R^2 with 0.3.

The upper two samples SYX13 and SYX16 show AHe ages ranging from 19.1 ± 2.4 to 37.7 ± 3.2 Ma, and from 13.9 ± 1.1 to 44.2 ± 4.3 Ma (Fig. 7a). The samples below ~2,500 m elevation yielded mean ages of 10 ± 1.9 and 12.4 ± 1.5 Ma. The age–elevation plot suggests a negative relationship; however, the mean AHe ages are similarly within error and indicate a rapid uplift and exhumation at ~10 Ma (Fig. 7). The lowermost sample (SYX11) at the transect shows large scatter in single-grain AHe ages ranging from 5.4 ± 0.4 to 30.1 ± 3.1 Ma (Table 1). Due to the fact that the zircons of the same sample yielded a well-reproduced 11.1 ± 0.6 Ma ZHe age, we assume that the two older AHe ages were influenced by parentless helium from microinclusions. Thus, two potential causes should be considered to account for the significantly scattered AHe ages in the upper two samples.

The first one is that those samples with poor quality, e.g., microinclusions, indicating the single-grain ages >~20–30 Ma (the ZHe ages of the upper two samples), e.g., SYX13-2a and SYX16-3a, are probably influenced by the microinclusions. The second is that a long residence time in the AHe PRZ between ~10 and 20 Ma, diffusion magnified the difference in He concentration and resulted in a large variation in AHe ages, which was followed by a rapid uplift and exhumation at ~10 Ma. The lowermost sample (SYX11) with ZHe age of 11.1 ± 0.6 Ma indicates that the sample was above 160–200 °C at ~10 Ma. There is ~1500 m elevation difference across the Mianshan transect, with a 40–60 °C variation in temperature—slightly smaller than the difference between the apatite HePRZ (50–80 °C) and zircon HePRZ (160–200 °C). It means that the uppermost sample was probably located around the apatite HePRZ. Excluding the single-grain AHe ages >~30 Ma in the upper two samples, those samples still have large scatter in replicate ages (Fig. 7a). Thus, we prefer the second cause for interpretation of the variation in AHe ages, although some grains were not completely suitable for helium dating. Such an interpretation could be further resolved by apatite fission track dating.

Fig. 2 Simplified geologic map, structural profile, reconstructed ▸ stratigraphic column, and sample location of the Xide transect. The error in estimated stratigraphic thickness and sample location could be up to ~100 m

Using the difference in the AHe and ZHe cooling ages (1.7–7.0 Ma) and the difference in the closure temperatures of the two systems, the data indicate rapid exhumation after 10 Ma with cooling at rates of ~24 °C/Ma (~0.8 mm/year), following a protracted denudation during ~20–10 Ma with rate of ~$0.15^{+INF}/_{-0.12}$ mm/year (Fig. 7b).

Wudu and Wushihe transects

The Wushihe and Wudu transects are located along the Dadu River (Fig. 5c, b), where twelve ZHe samples were collected. The ZHe ages in the Wudu transect range from 15.4 ± 3.0 to 64.8 ± 7.4 Ma (Table 1). The uppermost sample, SS04, shows significant scatter in replicate ages. Samples below ~1,200 m show a negative age–elevation relationship ($-1.89^{+1.9}/_{-41}$ mm/year), yet even so the scatter between single-grain ages is large (Fig. 7), indicating a rapid uplift and exhumation at ~20 Ma. It could be probably correlated to the deformation along the fault, as tilt related to deformation could result in such negative age–elevation relationship (Stockli 2005; Lee et al. 2013). The sample SS06 in the middle of the Wudu transect has single-grain ZHe ages ranging from 135 ± 14.6 to 484 ± 50.3 Ma, substantially older than the rapid cooling age and younger than the crystallization ages, which were probably influenced by the parentless helium.

The ZHe ages in the Wushihe transect yielded mean ages ranging from 2.9 ± 2.7 to 8.9 ± 3.3 Ma. Some of the single ZHe ages that are very old (from 192 ± 15.7 to 1,304 ± 140.5 Ma; Table 1; Fig. 7d) may reflect parentless helium from fluid inclusions. Moreover, one additional AHe age from a sample collected on the Dadu River, 20 km east of the main transect at ~580 m (sample SS12 in Fig. 5c), shows single-grain AHe age from 9.3 ± 1.1 to 22.1 ± 0.6 Ma, with a mean age of 15.7 ± 6 Ma. The age–elevation relationship of the Wushihe granite samples suggests an apparent exhumation rate of $0.35^{+INF}/_{-0.11}$mm/year from ~10 to 5 Ma (Fig. 7d). However, the sample SS20 yielded very young ages of 0.4 ± 0.7 to 2.7 ± 0.6 Ma, which could be caused by local thrusting or ground-hot-water flow (Whipp and Ehlers 2007), given there is no volcanicities occurred during Late Cenozoic times across the sampled area.

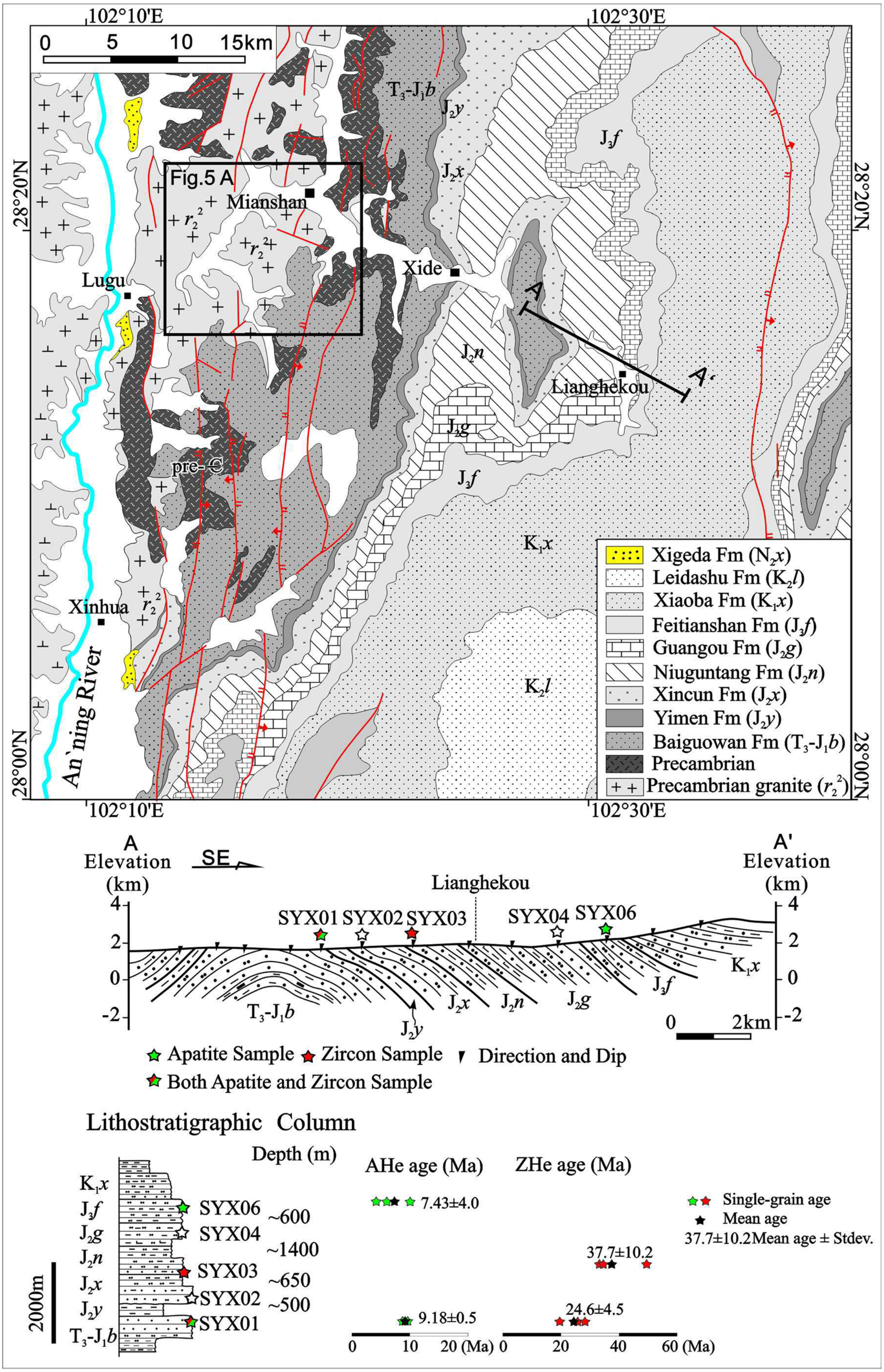

102°10'E
102°30'E
0 5 10 15km
28°20'N
28°00'N
Fig.5 A
Mianshan
Xide
Lugu
Lianghekou
Xinhua
An`ning River
pre-Є
A
A'
Xigeda Fm (N2x)
Leidashu Fm (K2l)
Xiaoba Fm (K1x)
Feitianshan Fm (J3f)
Guangou Fm (J2g)
Niuguntang Fm (J2n)
Xincun Fm (J2x)
Yimen Fm (J2y)
Baiguowan Fm (T3-J1b)
Precambrian
Precambrian granite (r22)
Elevation (km)
SE
SYX01 SYX02 SYX03
SYX04 SYX06
0 2km
Apatite Sample
Zircon Sample
Direction and Dip
Both Apatite and Zircon Sample
Lithostratigraphic Column
Depth (m)
AHe age (Ma)
ZHe age (Ma)
~600
~1400
~650
~500
2000m
7.43±4.0
37.7±10.2
24.6±4.5
9.18±0.5
Single-grain age
Mean age
37.7±10.2Mean age ± Stdev.

Discussion

Variation of (U–Th)/He single-grain ages

Although most of the sample ages show consistency in replicates and a systematic relationship with structural depth/elevation, a few samples show a large scatter in replicate analyses (e.g., sample SQM11, SS23 and SS12, Table 1). Variations between sample replicates have been reported in an increasing number of studies and can be attributed to (1) parentless helium from microinclusion, (2) helium implantation, (3) radiation damages, and (4) zoning of U and Th (Fitzgerald et al. 2006; Flowers et al. 2007; Spiegel et al. 2009).

There are several anomalous ages that could be attributed to microinclusions, e.g., SS15_1z and SYX11_3a. It is difficult to dismiss the possible influence of poor quality of some samples that have affected the He ages. However, samples in the Muchuan and in the Mianshan transects show a systematic decrease in the spread of AHe and ZHe ages in a single grain, respectively (Figs. 6a, 7b). We thus do not consider microinclusions to be the predominant source of the observed scatter.

Spencer et al. (2004) suggested that the majority of the "too old" ages can be explained by helium implantation from surrounding U–Th-rich minerals and host sedimentary components. Spiegel et al. (2009) argued that He implantation is most pronounced in apatite with effective U concentration <5 ppm. Thus, most reliable results for AHe ages are probably attained from those samples where U concentrations are >5 ppm. We did not measure the U and Th concentration directly, but made a rough estimate of the effective U concentration in ppm by calculating the grain mass using the measured grain size and a 3.2 g/cm^3 apatite density. The result shows that the effective U concentrations are relatively high (between 10 and 300 ppm; Table 1), which makes the possibility of He implantation from its surrounding unlikely. Furthermore, we do not observe a correlation between U concentration and AHe ages (Fig. 8). This is opposite to the trend of increasing age with increasing effective U concentrations resulting from radiation-induced damage to the apatite structure, as described by Shuster et al. (2006) and Flowers et al. (2007). Thus, He implantation and radiation damage trapping can be excluded as explanations for the variation in ages.

The AHe and ZHe system is thought to be an open system at temperatures between ~50–80 and 160–200 °C, respectively (Wolf et al. 1998; Reiners and Brandon 2006). That means when a sample underwent slow cooling, or prolonged residence in the PRZ, diffusion could potentially magnify the difference in He concentration. This is particularly the case when each grain has slightly different U and Th distribution and/or different grain sizes, which results in a large variation between (U–Th)/He ages of replicates of the same sample (Farley 2000; Reiners and Farley 2001; Meesters and Dunai 2002; Fitzgerald et al. 2006). Furthermore, a very slow cooling rate could amplify any kinetic, anisotropy, or zonation effects in apatite and zircon (Hourigan et al. 2005; Reich et al. 2007; Flowers et al. 2007), which result in considerable age differences (Biswas et al. 2007). Furthermore, an age signature typical for slow cooling through the PRZ is observed in several samples located at the upper part of the profiles (i.e., SQM05 at the top of Muchuan transect). These samples are interpreted to represent an exhumed PRZ and allow the estimate of burial depth and exhumation (see below).

As for considerably scattered single-grain (U–Th)/He ages, Fitzgerald et al. (2006) suggested that the "true age" lies between the minimum (U–Th)/He age and the weighted mean age. However, most of the sample ages show consistency in replicates and a systematic relationship with structural depth/elevation. Only a few samples show a large scatter in replicate analyses with a range of 10–20 Ma, smaller than the variation suggested by Fitzgerald et al. (2006) with a range of 30–100 Ma. We thus argue that the mean (U–Th)/He age is more valid than the youngest single-grain age to represent sample age. The observed variation of replicate ages can be thus attributed to the thermal history of the sample characterized by a prolonged residence time in the PRZ.

Fig. 3 Simplified geological map, structure profile, reconstructed ▸ stratigraphic column, and sample location of Ganluo transect. The error associated with the stratigraphic thickness and sample location can be up to ~ 100 m

Estimates of burial depths and exhumation

There are various post-depositional (or burial) depths and exhumation magnitudes between the stratigraphic columns (T_3–J_1) indicated by the AHe and ZHe ages. Mean surface temperatures and proximal borehole thermal gradients represent the best available proxy for the current thermal field through which the samples cooled. More than seven measurements at the southwestern margin of the Sichuan Basin indicate a geothermal gradient of ~25–35 °C/km and a surface temperature of 20 °C (Hu et al. 2000; Xu et al. 2011). For the Muchuan transect, the partially reset ZHe ages indicate a maximum burial temperature of 160–200 °C for the T_3–J_1 strata. For this temperature, we estimated a maximum thickness of the overlying sedimentary column that has been removed of 4.5–6.4 km. Consequently, the Lower Cretaceous burial depth could not exceed ~2–3.5 km, which is roughly consistent with the observed paleo-AHe PRZ, which represents paleo-temperatures of 50–80 °C (Fig. 6). Given that there are ~0.8- to 1.5-km-thick Late

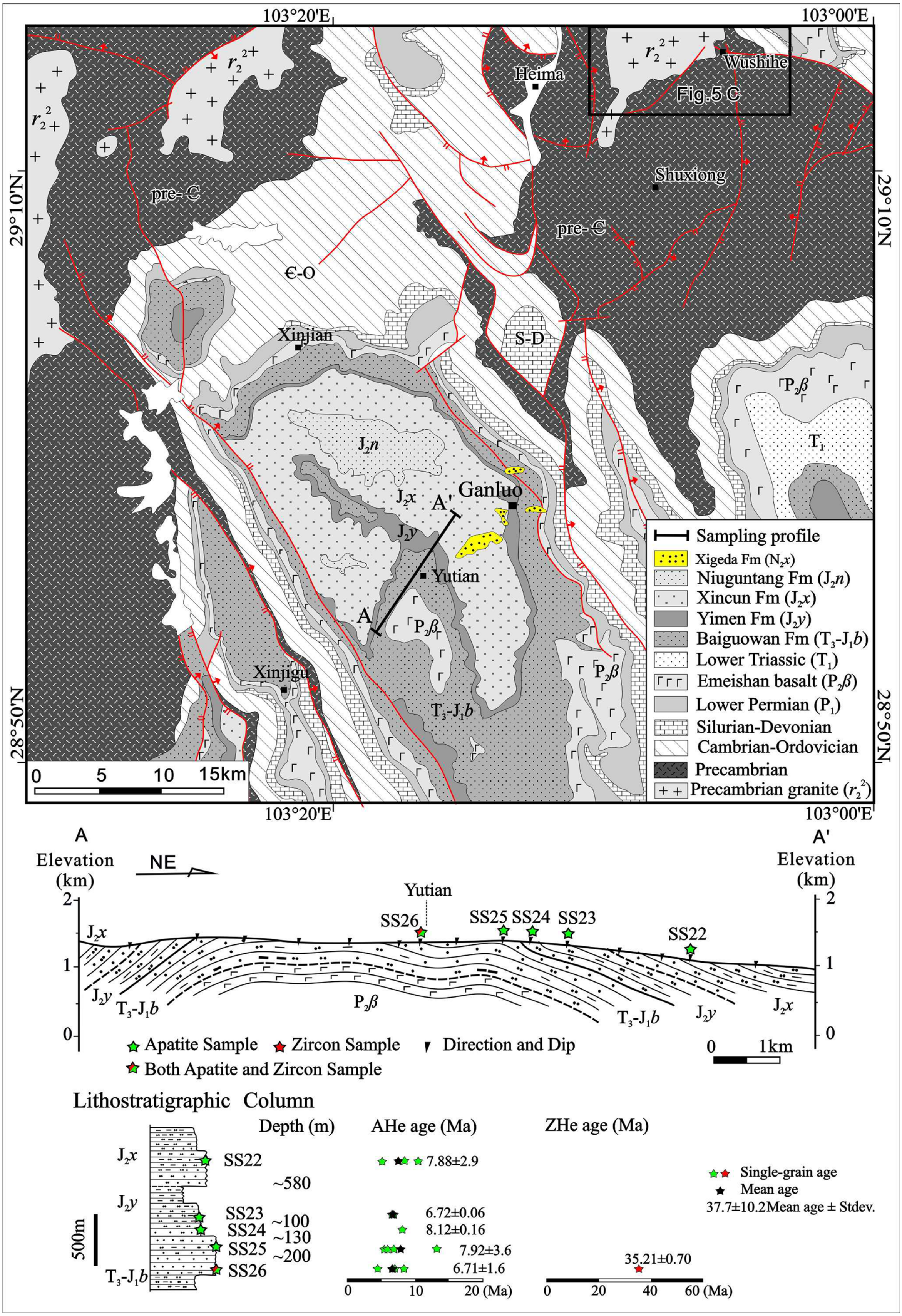

103°20'E
103°00'E
29°10'N
28°50'N
Heima
Wushihe
Fig.5 C
Shuxiong
pre-Є
Є-O
S-D
Xinjian
J_2n
J_2x
J_2y
A'
A
Ganluo
Yutian
$P_2\beta$
T_1
Xinjigu
T_3-J_1b
0 5 10 15km
Sampling profile
Xigeda Fm (N_2x)
Niuguntang Fm (J_2n)
Xincun Fm (J_2x)
Yimen Fm (J_2y)
Baiguowan Fm (T_3-J_1b)
Lower Triassic (T_1)
Emeishan basalt ($P_2\beta$)
Lower Permian (P_1)
Silurian-Devonian
Cambrian-Ordovician
Precambrian
Precambrian granite (r_2^2)
Elevation (km)
NE
Yutian
SS26
SS25
SS24
SS23
SS22
Apatite Sample
Zircon Sample
Direction and Dip
Both Apatite and Zircon Sample
0 1km
Lithostratigraphic Column
Depth (m)
AHe age (Ma)
ZHe age (Ma)
~580
~100
~130
~200
500m
7.88±2.9
6.72±0.06
8.12±0.16
7.92±3.6
6.71±1.6
35.21±0.70
Single-grain age
Mean age
37.7±10.2Mean age ± Stdev.
0 10 20 (Ma)
0 20 40 60 (Ma)

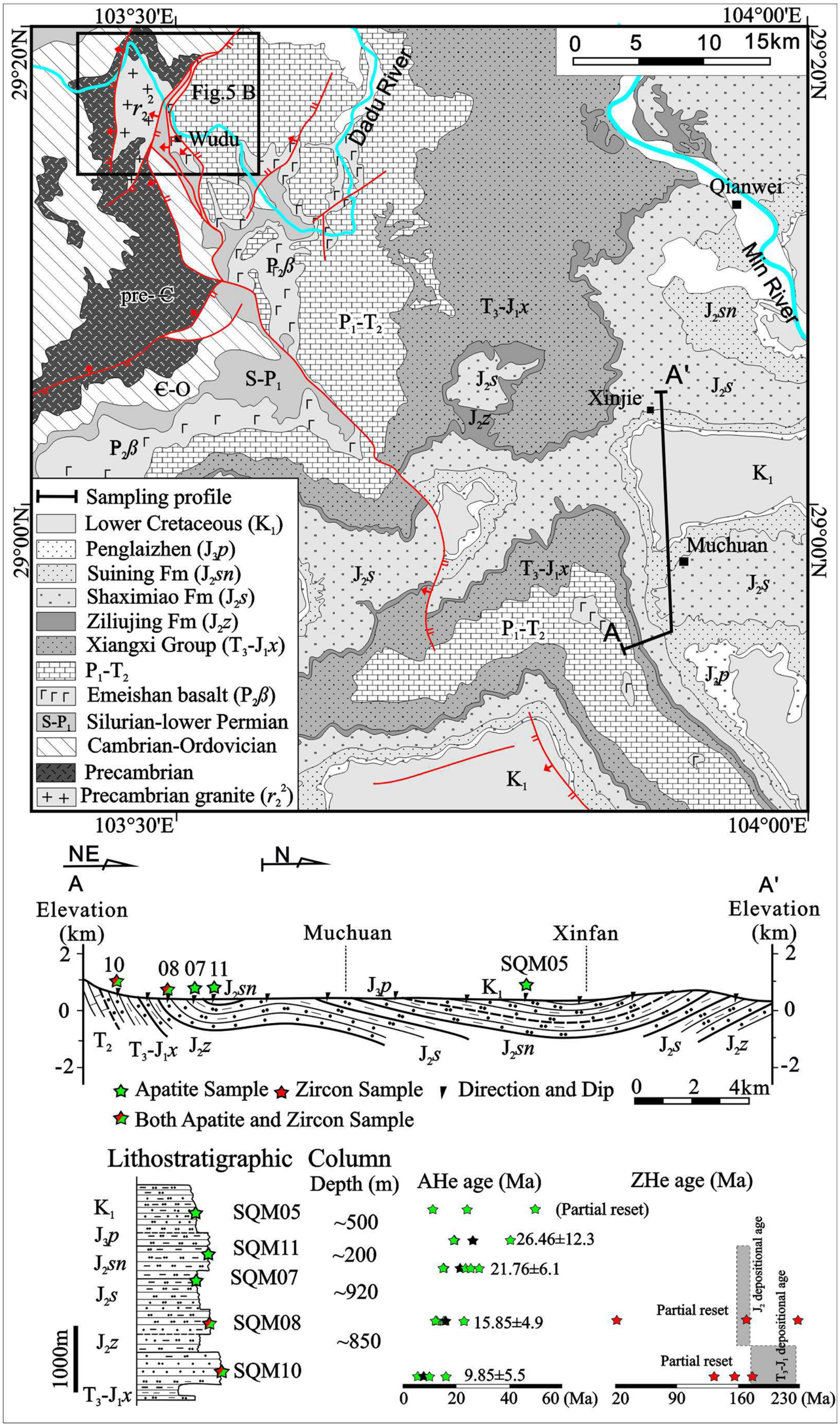

103°30'E
104°00'E
29°20'N
29°00'N
0 5 10 15km
Fig.5 B
Wudu
Dadu River
Qianwei
Min River
pre-Є
Є-O
S-P1
P2β
P1-T2
T3-J1x
J2s
J2z
J2sn
Xinjie
A'
A
K1
Muchuan
J3p
Sampling profile
Lower Cretaceous (K1)
Penglaizhen (J3p)
Suining Fm (J2sn)
Shaximiao Fm (J2s)
Ziliujing Fm (J2z)
Xiangxi Group (T3-J1x)
P1-T2
Emeishan basalt (P2β)
Silurian-lower Permian
Cambrian-Ordovician
Precambrian
Precambrian granite (r2^2)
NE
N
Elevation (km)
Muchuan
Xinfan
SQM05
10
08 07 11
T2
Apatite Sample
Zircon Sample
Direction and Dip
Both Apatite and Zircon Sample
0 2 4km
Lithostratigraphic Column
Depth (m)
AHe age (Ma)
ZHe age (Ma)
SQM05 ~500
SQM11 ~200
SQM07 ~920
SQM08 ~850
SQM10
1000m
(Partial reset)
26.46±12.3
21.76±6.1
15.85±4.9
9.85±5.5
Partial reset
J2 depositional age
T3-J1 depositional age
0 20 40 60 (Ma)
20 90 160 230 (Ma)

◂ **Fig. 4** Simplified geological map, structure profile, reconstructed stratigraphic column, and sample locations at the Muchuan transect. The error associated with stratigraphic thickness can to be up to ~200 m

Cretaceous deposits in the region today (BGMRSP 1991; Guo et al. 1996), we suggested that ~1- to 2-km-thick Tertiary strata must have been eroded during the Late Cenozoic, and a ~1–2 km exhumation occurred here.

The fully reset ZHe ages found at the bottom of the stratigraphic profile of the two other transects (Xide and Ganluo) suggest a minimum exhumation magnitude ranging from 4.2 to 5.6 km, assuming a paleo-geothermal gradient of 30–40 °C/km and surface temperature of 10 °C across much of the Daliang Mountains (Hu et al. 2000). The burial depths of the present surfaces (K_2 and J_2) are thus greater than ~1–2 and ~3–4 km in the Xide and Ganluo transects, respectively. According to the exhumation magnitude at the base of each column equal to a sum of the surface denudation, the reconstructed depth and the preserved strata overlying the columns, the estimates of ~1.8–3.5 and ~2.8–5.2 km probably represent a suitable exhumation at the Xide and Ganluo transects. This conclusion is based on (1) the reconstructed depths in each stratigraphic column have up to ~0.2–0.5 km difference than regionally averaged stratigraphic thicknesses, (2) the assumption of ~1- to 2-km-thick Tertiary section is based on the Muchuan transect, and (3) the regionally preserved thicknesses of ~0.5–1.2 km and ~0.5 km in the Lower Cretaceous and Upper Jurassic (BGMRSP 1991; Guo et al. 1996). Furthermore, the exhumed AHe PRZ in the Mianshan granite indicates an exhumation magnitude of ~1.0–2.5 km. We argue that ~2.5 and ~5 km are the best estimates of the Late Cenozoic exhumation magnitude for the Xide and Ganluo transects, respectively. Exhumation near the margin of the Sichuan Basin is characterized by much smaller amounts of denudation (~1–2 km in the Muchuan transect). It should be noted that the estimated exhumation in transects could significantly change due to new information on changes of deposits thickness (e.g., intermountain basin), deformation and thrusting along faults (e.g., growth strata), etc.

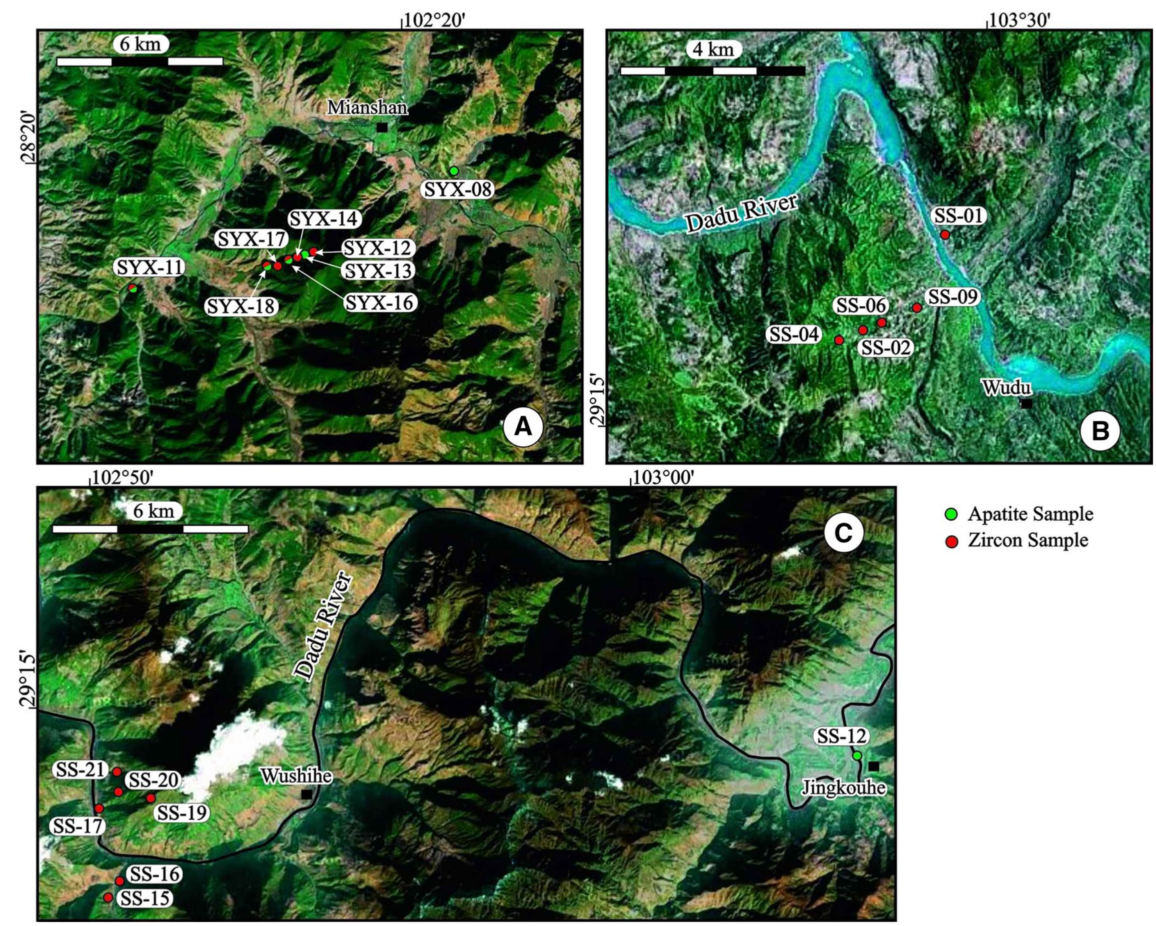

Fig. 5 Sample location maps for the Mianshan granite (**a**), Wudu granite (**b**) and Wushihe granite (**c**). Topography maps are from Google Earth

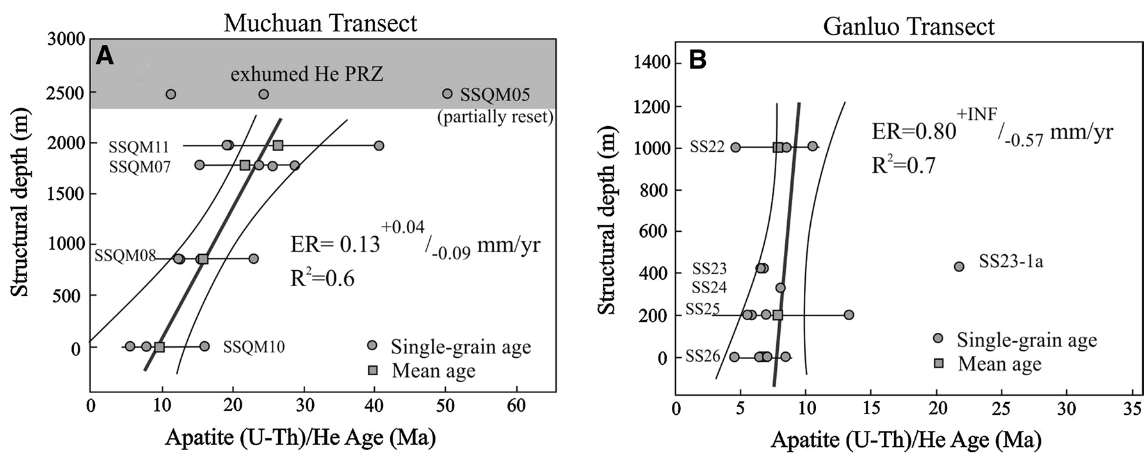

Fig. 6 Plots of age versus structural depth relationships for **a** Muchan and **b** Ganluo transects. The *bold lines* define apparent exhumation rates (ER) with 95 % confidence intervals

Two-phase exhumation of the Daliang Mountains

Documenting exhumation intensity, as well as its spatial and temporal variations, is important for understanding regional patterns of denudation. The Muchuan, Ganluo, Mianshan, and Xide transects show a similar exhumation rate of ~0.15 mm/year from ~30 to 10 Ma. Most of the transects (e.g., the Wushihe, Ganluo, Xide, Mianshan, and Wudu transects) show a faster rate of ~0.4–0.8 mm/year (or a negative elevation vs. age relationship) since 10 Ma (Fig. 9). The regional consistency of these data suggests that the Daliang Mountains experienced a protracted period of slow cooling and exhumation before ~10 Ma, then an accelerated cooling and exhumation during Late Miocene time.

Due to the lack of Cenozoic depositional records in the region, the deformation and Cenozoic uplift in the southwestern part of the Sichuan Basin are not well constrained, although thermochronometric data have recently revealed that episodic exhumation played a key role in shaping the topography (An et al. 2008; Richardson et al. 2008; Deng et al. 2009; Li et al. 2012). The deformation of the youngest Upper Cretaceous strata demonstrates that the main deformation in the Daliang Mountains occurred post Cretaceous (Figs. 2, 3, 4), consistent with no significant change in the paleocurrent and sedimentary facies across much of the intermontane basins in the Daliang Mountains (e.g., Ganluo and Jiuxiang Basins) during Late Triassic to Jurassic times (Chen et al. 2011). Those folded precretaceous strata were overlain by undeformed Late Cenozoic strata (i.e., Neogene Xigeda Fm). Recently, Zhao et al. (2008) and Kong et al. (2009, 2012) argued that the Xigeda Formation has an age of ~1.5–8.7 Ma, according to magneto-stratigraphic research and cosmogenic ^{10}Be and ^{26}Al dating. In particular, there is only nonconformity to low-angle unconformity developed during Jurassic to Paleogene sedimentary deposition, across the Daliang Mountains and the southwestern Sichuan Basin (BGMRSP 1991; Guo et al. 1996; Deng et al. 2012b). Thus, we argue that the main phase of deformation in the Daliang Mountains probably occurred in the Late Miocene, post-dating the protracted period of slow cooling and exhumation.

The protracted process is consistent with an erosional response to broad regional uplift (Richardson et al. 2008; Wilson and Fowler 2011; Wang et al. 2012a; Li et al. 2012; Deng et al. 2013). It can be correlated with an increase in stream incision on the plateau margin (Clark et al. 2004; Wilson and Fowler 2011) or with a base-level fall in the adjacent Sichuan Basin (Richardson et al. 2008), where 1.5–4 km of strata was eroded by the Yangtze river (Richardson et al. 2010; Deng et al. 2013). Based on the apatite fission track and (U–Th)/He data, Richardson et al. (2008), Li et al. (2012), and Deng et al. (2013) argued that major regional erosion has not started earlier than ~40–20 Ma ago. This timing of Cenozoic erosion is consistent with our oldest ZHe age that displays cooling at 37.7 ± 10 Ma (i.e., Xide transect). It resulted to thick deposits of gypsum and mirabilite across the southwestern Sichuan Basin during Paleogene times (e.g., Shuangliu and Minshan area in the southwest of Sichuan Basin), indicating that a connection between the Sichuan Basin and the Panzhihua–Xichang area was closed and the southwestern Sichuan Basin became an interior basin (BGMRSP 1991; Guo et al. 1996). Later, the connection of the Sichuan Basin to the South China Sea or East China Sea has been established, but different hypotheses were proposed for the timing of this opening (Clark et al. 2004; Xiang et al. 2007; Richardson et al. 2010).

Late Cenozoic deformation and rapid exhumation across the Daliang Mountains

East–west compression as a far-field effect of Indo-Eurasia convergence has accommodated widespread deformation to form those nearly N–S striking structures, including

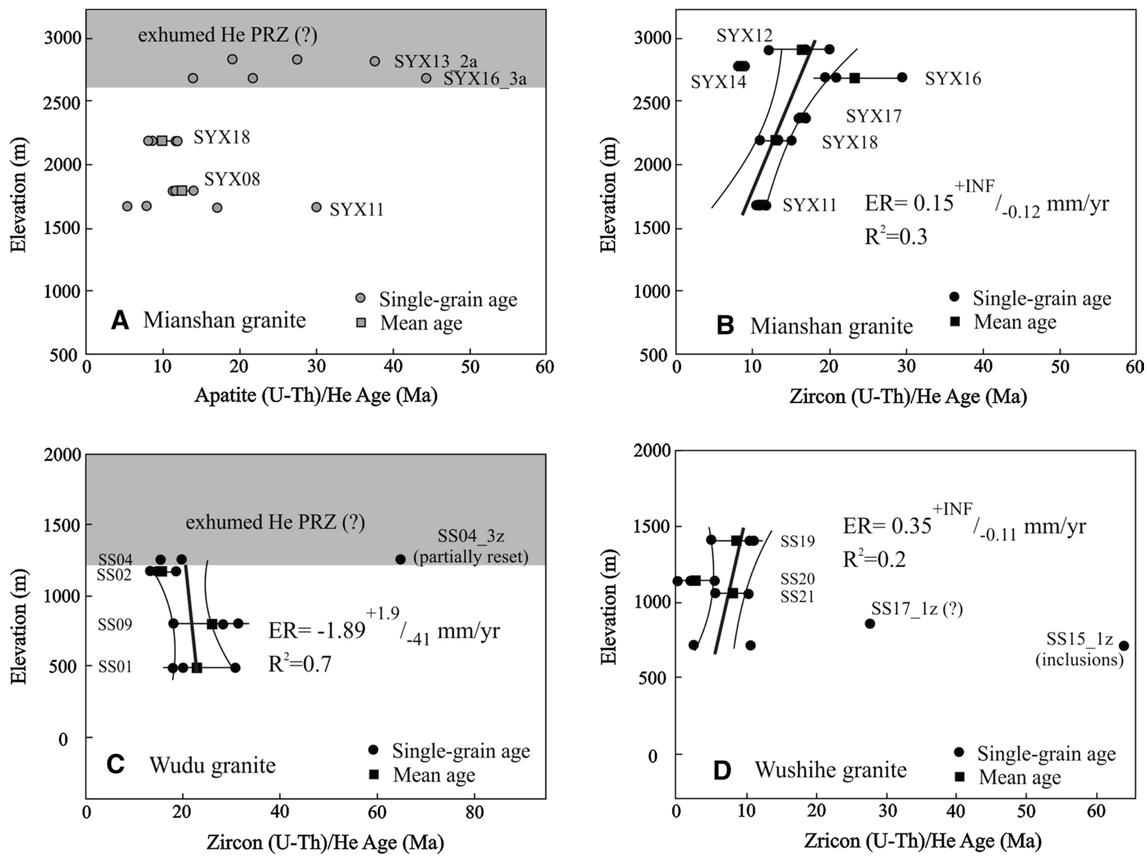

Fig. 7 Plots of age–elevation relationships for **a**, **b** Mianshan, **c** Wudu, and **d** Wushihe transects. The *bold lines* define apparent exhumation rates with 95 % confidence intervals

anticlines (e.g., the Ganluo and Xide anticline), synclines, and faults (BGMRSP 1991; Burchfiel et al. 1995; Wang and Yin 2009); for example, the Jinping thrust belt (shown as Jinping Mts. in Fig. 1) thrusts on the footwall of Oligocene–Miocene strata during this time indicated by apatite fission track ages (Wang et al. 2012b). Kinematic studies on the southeastern margin of the Tibetan Plateau show that the Xianshuihe fault is characterized by ~60–80 km left-lateral offset and that the Xiaojiang fault show a ~48–60 km offset (Burchfiel et al. 1995; Wang et al. 1998). Southeastward displacement of the southern part of the Songpan–Ganzi fold belt (e.g., Yajiang Terrane) and in particular the Xianshuihe fault (with at least a ~10–20 km offset) was absorbed by deformation in the Daliang Mountains (Wilson et al. 2006; Wang and Yin 2009). Based on a balanced cross section, Chen and He (2008) suggested a crustal shortening of 17.8 % during Miocene–Pliocene time, with an average shortening of ~11 km in the Daliang Mountains and its western margin (e.g., the Qinghe area with a shortening of ~20 %, Wang et al. 2012b). We thus argue that rapid cooling and exhumation occurred coevally in the Daliang Mountains (e.g., Ganluo and Mianshan sections, Wushihe granite).

The estimated post ~10-Ma exhumation rates (~0.4–0.8 mm/year) across the Daliang Mountains are similar to rates of 0.25–0.5 mm/year suggested for the Songpan–Ganzi region for the same time (Clark et al. 2005; Ouimet et al. 2010). Furthermore, a similar timing in the onset of rapid denudation is observed across much of the eastern margin of the Tibetan Plateau, e.g., the Longmen Shan at 5–15 Ma (Kirby et al. 2002; Godard et al. 2009a; Wang et al. 2012a), the Gonga Shan at ~12 Ma (Roger et al. 1995; Zhang et al. 2004a), and the western Qinling at 9–4 Ma (Enkelmann et al. 2006). It suggests that this rapid exhumation is due to the eastward growth of the Tibetan Plateau and its associated uplift and erosion.

The Indo–Eurasia collision resulted in crustal material being extruded and rotated clockwise around the eastern Himalayan syntaxis (Fig. 1). The region between the syntaxis and the Xianshuihe–Xiaojiang fault system is extruded southeastward in an inhomogeneous and diachronous process during the Late Cenozoic (Wang et al. 1998; Burchfiel and Wang 2003). The plateau growth toward the southeast is mainly accommodated by large strike-slip fault zones like the Xianshuihe–Daliangshan strike-slip fault (e.g.. Tapponnier et al. 2001; Wilson et al. 2006), which

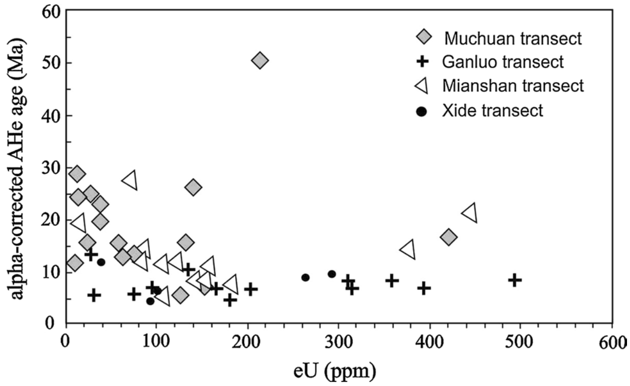

Fig. 8 Relationship between AHe ages and effective U concentrations in different transects

is thought to be active since at least ~12–5 Ma (Roger et al. 1995; Xu and Kamp 2000; Zhang et al. 2004a). Furthermore, widespread occurrence of flower structures suggest that the deformation is mainly accommodated with transpression along strike-slip faults (e.g., Xianshuihe fault, Mopanshan fault) in the Daliang Mountains. Most of the transects in our study area that have the youngest AHe ages are located in the hanging wall of Daliangshan and Anlinghe faults (i.e., Ganluo and Xide transects, Mianshan and Wushihe granites, Figs. 1, 9), where there occurred rapid exhumation with gentle-to-moderate deformation. Due to eastward growth of the Tibetan Plateau and its compression, widespread eastward thrusting structures (e.g., the Mabian fault) and NWW to S–N striking structures around the southwestern Sichuan Basin developed (Chen et al. 2011; Wilson et al. 2006; Wang et al. 2012b). It suggests that rapid exhumation in the Wudu granite can be correlated with the deformation at the Mabian fault, which is consistent with the Late Cenozoic architecture of the southwestern Sichuan Basin (An et al. 2008; Liu et al. 2012).

Notwithstanding, there is some geophysical evidence (Xu et al. 2007; Bai et al. 2010) to support a lower crustal

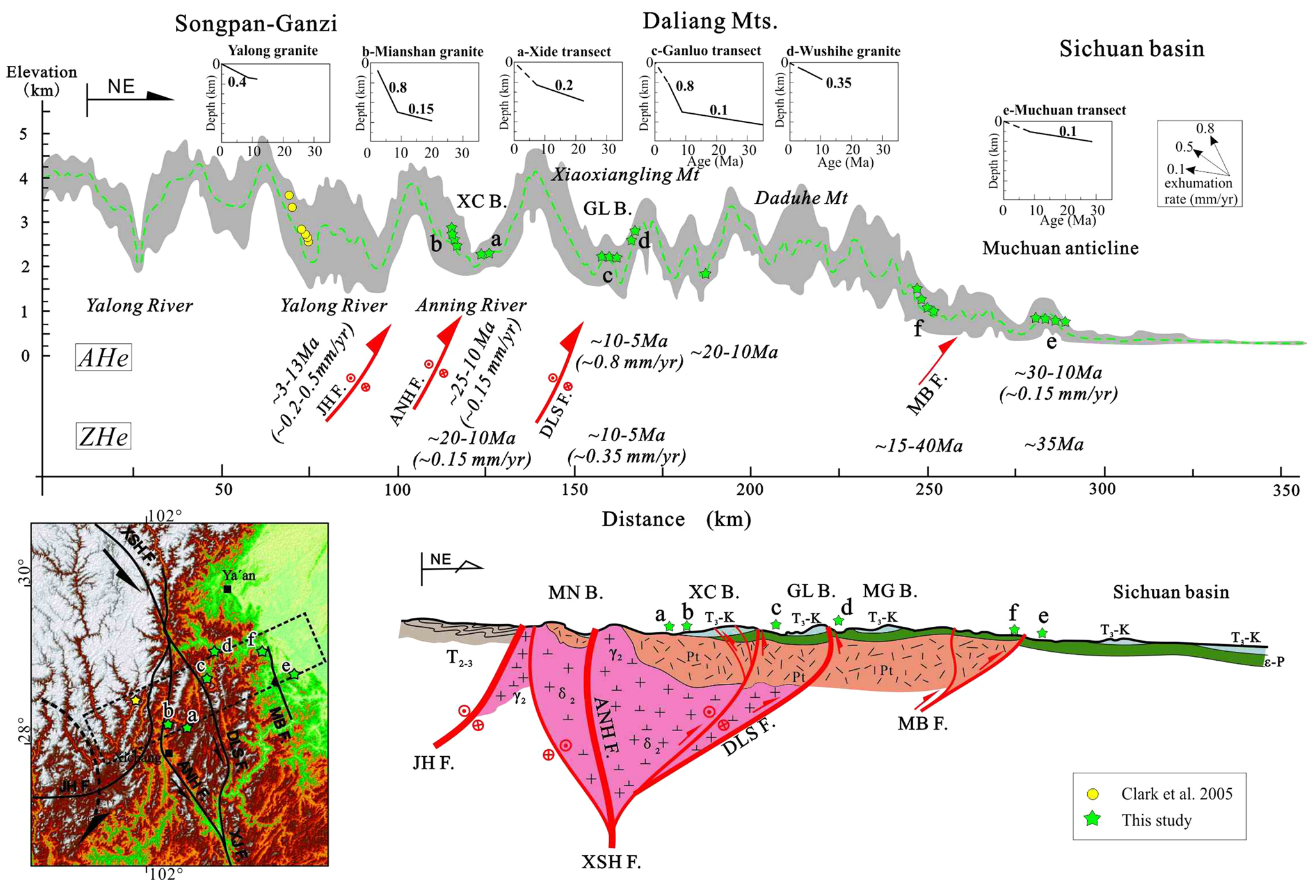

Fig. 9 Tectonics transect across the southeastern margin of the Tibetan Plateau and the Daliang Mountains to show the relationship between the topography, the (U–Th)/He ages, and exhumation rates. AHe and ZHe ages show the range of single-grain ages (*yellow circles* and *star* from Clark et al. (2005) and *green stars* are this study). *a* Xide transect, *b* Mianshan granite, *c* Ganluo transect, *d* Wushihe granite, *e* Muchuan transect, *f* Wudu granite. XSH F.—Xianshuihe fault, DLS F.—Daliangshan fault, ANH F.—Anninghe fault, XJ F.—Xiaojiang fault, JH F.—Jinghe fault, MB F.—Mabian fault, MN B.—Miannin Basin, XC B.—Xichang Basin, GL B.—Ganluo Basin, MG B.—Meigu Basin. It should be noted that there is a distinct boundary on Daliangshan fault with an apparent exhumation rate of 0.4–0.8 mm/year from ~10 to 5 Ma

channel flow that caused surface uplift and exhumation across the eastern Tibetan Plateau. A consistent pattern of exhumation without anomalously uplifted areas as in the studies of Clark et al. (2005) and Enkelmann et al. (2006) is observed across the Daliang Mountains, even across much of southeastern Tibet (Wilson and Fowler 2011). Furthermore, geological studies indicated a significant amount of shortening and deformation (Chen and He 2008; Wang et al. 2012b). Thus, our results of accelerated denudation in the Daliang Mountains (post ~10 Ma) require a tectonic explanation of denudation, as related to eastward growth of the Tibetan Plateau. It is accommodated by the boundary strike-slip faults (Fig. 9) and crustal shortening accompanied with transpression as a primary driver for uplift and topography of the Daliang Mountains. It should be noticed that we did not rule out the lower crustal channel flow here, as we argued that a crustal shortening is more significant than the lower crustal channel flow for surface exhumation in the Daliang Mountains .

Pattern of erosion rates across the southeastern margin of the Tibetan Plateau shows a strong gradient in exhumation rates with the highest rates at the eastern Himalayan syntaxis and a decrease toward the southeastern margin of the plateau (Henck et al. 2011). At the southeastern plateau margin, exhumation studies reveal a general eastward increase in cooling ages and a decrease in exhumation rate and amount toward the boundary strike-slip fault in the Daliang Mountains (Fig. 9). To the east of the strike-slip system, there is a broad consistency in AHe and ZHe ages and exhumation rates. The Muchuan transect at the southwestern margin of the Sichuan Basin shows a slower exhumation rate and smaller amount (~1–2 km) than others. It indicates significant differences in apatite and zircon He ages, exhumation rates and amounts between the Daliang Mountains and the Sichuan Basin. These strike-slip faults are thus interpreted to be the northernmost part of a NW-trending boundary between the southeastern Tibetan Plateau and the Sichuan Basin (even the South China block), controlled by a crustal fragment rotating clockwise around the eastern Himalayan syntaxis.

Conclusions

A positive age–depth correlation in restored stratigraphic column and age–elevation profiles are interpreted with respect to the denudation history of the Daliang Mountains. The Daliang Mountains record a period of slow cooling and exhumation during the Cenozoic with apparent exhumation rates of ~0.15 mm/year from ~30 to 10 Ma. This protracted slow cooling was followed by accelerated exhumation with rates ~0.4–0.8 mm/year during the Late Miocene. The post ~10-Ma rapid cooling and exhumation, we have attributed to the transpressional strike-slip faulting at the Xianshuihe–Xiaojiang fault system that resulted from the southeastward growth of the Tibetan Plateau. Our results thus support the hypothesis that mountain building in the Daliang is mainly caused by crustal shortening accompanied by transpression, rather than the previously suggested lower crustal channel flow. Based on the stratigraphy of the transects and the AHe and ZHe ages, we estimate the maximum burial depths and exhumation amount to be ~3–5 km in the Daliang Mountains and ~1–2 km at the margin to the Sichuan Basin.

Acknowledgments This work was supported by the National Natural Science Foundation of China (NSFC) under Grant Nos. 41402119, 2014JQ0057, 41472017, 41230313, and the National Basic Research Program of China (No. 2012CB214805). We would like to express our gratitude to Richard Lease and Saeed Madanipour for their helpful discussions, and to Frank Thomas for his help with English in the manuscript. We wish to extend our most sincere gratitude to Annika Szameitat, Cao Luo, Cong Tang and Ziha Mise for their assistance in the field and sample preparation.

References

An YF, Han ZJ, Wan JL (2008) Fission track dating of the Cenozoic uplift in Mabian area, southern Sichuan Province, China. Sci China Ser D Earth Sci 51:1238–1247

Arne D, Worley B, Wilson C, Chen SF, Foster D, Luo ZL, Liu SG, Dirks P (1997) Differential exhumation in response to episodic thrusting along the eastern margin of the Tibetan Plateau. Tectonophysics 280:239–256

Bai DH, Unsworth MJ, Meju MA, Ma XB, Teng JW, Kong XR, Sun Y, Sun J, Wang LF, Jiang CS, Zhao CP, Xiao PF, Liu M (2010) Crustal deformation of the eastern Tibetan plateau revealed by magnetotelluric imaging. Nature Geosciences. doi:10.1038/NGEO830

BGMRSP (Bureau of Geology and Mineral Resources of Sichuan Province) (1991) Regional Geology of Sichuan Province. Geological Publishing House, Beijing, pp 1–735

Biswas S, Coutand I, Grujic D, Hager C, Stöckli D, Grasemann B (2007) Exhumation and uplift of the Shillong plateau and its influence on the eastern Himalayas: new constraints from apatite and zircon (U–Th–[Sm])/He and apatite fission track analyses. Tectonics 26:TC6013. doi:10.1029/2007TC002125

Burchfiel BC, Wang E (2003) Northwest-trending, middle Cenozoic, left-lateral faults in southern Yunnan, China, and their tectonic significance. J Struct Geol 25:781–792

Burchfiel BC, Chen ZL, Liu ZP, Royden LH (1995) Tectonics of the Longmen Shan and adjacent regions, central China. Int Geol Rev 37:661–735

Chen CY, He HL (2008) Crustal shortening of Daliangshan tectonic zone in Cenozoic era and its implication. Seismology and Geology 30:443–453

Chen SF, Wilson CJL, Deng QD, Zhao XL, Luo ZL (1994) Active faulting and block movement associated with large earthquakes in Min Shan and Longmen Mountains, northeastern Tibetan Plateau. J Geophys Res 99:24025–24038

Chen SF, Wilson CJL, Worley BA (1995) Tectonic transition from the Songpan-Garze Fold Belt to the Sichuan Basin, south-western China. Basin Res 7:235–253

Chen H, Hu JM, Qu HL, Wu GL (2011) Early Mesozoic structural deformation in the Chuandian N–S tectonic belt, China. Sci China Earth Sci 54:1644–1651

Clark MK, Royden LH (2000) Topographic ooze: building the eastern margin of Tibet by lower crustal flow. Geology 28:703–706
Clark MK, Schoenbohm LM, Royden LH, Whipple KX, Burchfiel BC, Zhang X, Tang W, Wang E, Chen L (2004) Surface uplift, tectonics, and erosion of eastern Tibet from large-scale drainage patterns. Tectonics 23. doi:10.1029/2002TC001402
Clark MK, House MA, Royden LH, Whipple KX, Burchfiel BC, Zhang X, Tang W (2005) Late Cenozoic uplift of southeastern Tibet. Geology 33:525–528
Copley A (2008) Kinematics and dynamics of the southeastern margin of the Tibetan Plateau. Geophys J Int 174:1081–1100
Deng B, Liu SG, Liu S, Li ZW, Zhao JC (2009) Restoration of exhumation thickness and its significance in Sichuan basin, China. J Chengdu University Technol Sci Technol Ed 36:675–686
Deng B, Liu SG, Jansa LF, Cao JX, Cheng Y, Li ZW, Liu S (2012a) Sedimentary record of Late Triassic transpressional tectonics of the Longmenshan thrust belt, SW China. J Asian Earth Sci 48:43–55
Deng B, Liu SG, Li ZW, Cao JX, Sun W (2012b) Late cretaceous tectonic change of the eastern margin of Tibetan Plateau: results from multi-system thermochronology. J Geol Soc India 80:241–254
Deng B, Liu SG, Li ZW, Jansa L, Liu S, Wang GZ, Sun W (2013) Differential exhumation in the Sichuan Basin, eastern margin of Tibetan Plateau, from apatite fission-track thermochronology. Tectonophysics 591:98–115
Dirks P, Wilsion CJL, Chen S, Luo ZL, Liu S (1994) Tectonic evolution of the NE margin of the Tibetan Plateau; evidence from the central Longmen Mountains, Sichuan Province, China. J SE Asian Earth Sci 9:181–192
Enkelmann E, Ratschbacher L, Jonchheere R, Nestler R, Fleischer M, Gloaguen R, Hacker BR, Zhang YQ, Ma YS (2006) Cenozoic exhumation and deformation of northeastern Tibet and the Qinling: Is Tibetan lower crustal flow diverging around the Sichuan Basin. GSA Bulletin 6:651–671
Farley KA (2000) Helium diffusion from apatite: general behavior as illustrated by Durango fluorapatite. J Geophys Res 105:2903–2914
Farley KA, Wolf RA, Silver LT (1996) The effects of long alpha-stopping distances on U–Th/He dates. Geochim Cosmochim Acta 60:4223–4230
Fitzgerald PG, Baldwin SL, Webb LE, O'Sullivan PB (2006) Interpretation of (U–Th)/He single grain ages from slowly cooled crustal terranes: a case study from the Transantarctic Mountains of southern Victoria Land. Chemical Geology 225:91–120
Flowers R, Shuster D, Wernicke B, Farley K (2007) Radiation damage control on apatite (U–Th)/He dates from the Grand Canyon region, Colorado Plateau. Geology 35:447–450
Godard V, Pik R, Lave J, Cattin R, Tibari B, Sigoyer J D, Pubellier M, Zhu J (2009a) Late Cenozoic evolution of the central Longmen Shan, eastern Tibet: Insight from (U–Th)/He thermochrolometry. Tectonics 28. doi:10.1029/2008TC002407
Godard V, Lave J, Carcaillet J, Cattin R, Bourles D, Zhu J (2009b) Spatial distribution of denudation in Eastern Tibet and regressive erosion of plateau margins. Tectonophysics. doi:10.1016/j.tecto.2009.10.026
Guo ZW, Deng KL, Han KY (1996) Formation and Evolution of the Sichuan Basin. Geologic Publishing House, Beijing, pp 1–201
He B, Xu YG, Huang XL, Luo ZY, Shi YR, Yang QJ, Yu SY (2007) Age and duration of the Emeishan flood volcanism, SW China: Geochemistry and SHRIMP zircon U-Pb dating of silicic ignimbrites, post-volcanic Xuanwei Formation and clay tuff at the Chaotian section. Earth Planet Sci Lett 255:306–323
He HL, Ikeda Y, He YL, Togo M, Chen J, Chen CY, Tajikara M, Echigo T, Okada S (2008) Newly-generated Daliangshan Fault Zone—shortcutting on the central section of Xianshuihe–Xiaojiang fault system. Sci China Ser D Earth Sci 51:1248–1258
Henck AC, Huntington KW, Stone JO, Montgomery DR, Hallet B (2011) Spatial controls on erosion in the Three Rivers Region, southeastern Tibet and southwestern China. Earth Planet Sci Lett. doi:10.1016/j.epsl.2010.12.038
Hourigan JK, Reiners PW, Brandon MT (2005) U–Th zonation-dependent alpha-ejection in (U–Th)/He chronometry. Geochim Cosmochim Acta 69:3349–3365
Hu SB, He LJ, Wang JY (2000) Heat flow in the continental area of China: a new data set. Earth Planet Sci Lett 179:407–419
Hubbard J, Shaw JH (2009) Uplift of the Longmen Shan and Tibetan plateau, and the 2008 Wenchuan (M = 7.9) earthquake. Nature 458:194–197
Kirby E, Reiners PW, Krol MA, Whipple KX, Hodges KV, Farely KA, Tang WQ, Chen ZL (2002) Late Cenozoic evolution of the eastern margin of the Tibetan Plateau: inferences from $^{40}Ar/^{39}Ar$ and (U–Th)/He thermochronology. Tectonics 21. doi:10.1029/2000TC001246
Kong P, Granger DE, Wu FY, Caffee MW, Wang YJ, Zhao XT, Zheng Y (2009) Cosmogenic nuclide burial ages and provenance of the Xigeda paleo-lake: implications for evolution of the Middle Yangtze River. Earth Planet Sci Lett 278:131–141
Kong P, Zheng Y, Caffe MW (2012) Provenance and time constraints on the formation of the first bend of the Yangtze River. Geochem Geophys Geosyst 13:Q06017. doi:10.1029/2012GC004140
Lai QZ, Ding L, Wang HW, Yue YH, Cai FL (2007) Constraining the stepwise migration of the eastern Tibetan Plateau margin by apatite fission track thermochronology. Sci China Ser D Earth Sci 50:172–183
Lee JP, Stockli DF, Kelley SA, Pederson JL, Karlstrom KE, Ehlers TA (2013) New thermochronometric constraints on the Tertiary landscape evolution of the central and eastern Grand Canyon, Arizona. Geosphere 9:216–228
Li ZW, Liu SG, Chen HD, Deng B, Hou MC, Wu WH, Cao JX (2012) Spatial variation in Meso-Cenozoic exhumation history of the Longmen Shan thrust belt (eastern Tibetan Plateau) and the adjacent western Sichuan basin: constraints from fission track thermochronology. J Asian Earth Sci 47:185–203
Liu SG, Deng B, Li ZW, Sun W (2012) Architectures of Basin–Mountain Systems and their influences on gas distribution: a case study from Sichuan Basin, South China. J Asian Earth Sci 47:204–215
Liu SG, Ma YS, Sun W, Cai XY, Liu S, Huang WM, Xu GS, Yong ZQ, Wang GZ, Wang H, Pan CL (2008) Studying on the differences of Sinian natural gas pools between Weiyuan gas field and Ziyang gas-brone area, Sichuan Basin. Acta Geol Sin 82:328–337
Ludwig K (2003) Isoplot/Ex: a geochronological toolkit for Microsoft Excel, Spec. Publ. No. 1a. Berkeley Geochronology Center, Berkeley, CA, p. 56
Luo ZL (1998) New recognition of basement in Sichuan basin. J Chengdu Univ Technol 25:191–200
Meesters AA, Dunai TJ (2002) Solving the production diffusion equation for finite diffusion domains of various shapes: Part II. Application to cases with a-ejection and nonhomogeneous distribution of the source. Chem Geol 186:347–363
Mukherjee S (2005) Channel flow, ductile extrusion and exhumation of lower mid-crust in continental collision zones. Curr Sci 89:435–436
Ouimet WB, Whipple KX, Granger DE (2009) Beyond threshold hillslopes: channel adjustment to base-level fall in tectonically active mountain ranges. Geology 37:579–582
Ouimet W, Whipple K, Royden L, Reiners P, Hodges K, Pringle M (2010) Regional incision of the eastern margin of the Tibetan Plateau. Lithosphere 2:50–63
Reich M, Ewing RC, Ehlers TA, Becker U (2007) Low-temperature anisotropic diffusion of helium in zircon: implications for

zircon (U–Th)/He thermochronometry. Geochim Cosmochim Acta 71:3119–3130
Reiners PW, Brandon M (2006) Using thermochronology to understand orogenic erosion. Annu Rev Earth Planet Sci 34:419–466
Reiners PW, Farley KA (2001) Influence of crystal size on apatite (U–Th)/He thermochronology: an example from the Bighorn Mountains, Wyoming. Earth and Planetary Science Letters 188:413–420
Reiners PW, Zhou ZY, Ehlers TA, Xu CH, Brandon MT, Donelick RA, Nicolescu SN (2003) Post-orogenic evolution of the Dabie Shan, Eastern China, from (U–Th)/He and fission-tack thermochronology. Am J Sci 303:489–518
Reiners PW, Spell TL, Nicolescu S, Zanetti KA (2004) Zircon (U–Th)/He thermochronometry: He diffusion and comparisons with $^{40}Ar/^{39}Ar$ dating. Geochim Cosmochim Acta 68:1857–1887
Richardson NJ, Densmore AL, Seward D, Fowler A, Wipf M, Ellis MA, Li Y, Zhang Y (2008) Extraordinary denudation in the Sichuan Basin: Insights from low-temperature thermochronology adjacent to the eastern margin of the Tibetan Plateau. J Geophys Res 113. doi:10.1029/2006JB004739
Richardson NJ, Densmore AL, Seward D, Wipf M, Li Y (2010) Did incision of the Three Gorges begin in the Eocene? Geology 38:551–554
Roger F, Calassou S, Lancelot J, Malavieille J, Mattauer M, Zu ZQ, Hao ZW, Hou LW (1995) Miocene emplacement and deformation of the Konga Shan granite (Xianshui He fault zone, west Sichuan, China): Geodynamic implications. Earth Planet Sci Lett 130:201–216
Royden LH, Burchfiel BC, van der Hilst RD (2008) The geological evolution of the Tibetan Plateau. Science 321:1054–1058
Schoenbohm LM, Burchfiel BC, Chen LZ (2006a) Propagation of surface uplift, lower crustal flow, and Cenozoic tectonics of the southeast margin of the Tibetan Plateau. Geology 34:813–816
Schoenbohm L, Burchfiel BC, Chen LZ, Yin JY (2006b) Miocene to present activity along the Red River fault, China, in the context of continental extrusion, upper crustal rotation, and lower crustal flow. GSA Bulletin 118:672–688
Shen ZK, Lü JN, Wang M, Bürgmann R (2005) Contemporary crustal deformation around the southeast borderland of the Tibetan Plateau. J Geophys Res 110. doi:10.1029/2004JB003421
Shuster DL, Flowers R, Farley K (2006) The influence of natural radiation damage on helium diffusion kinetics in apatite. Earth Planet Sci Lett 249:148–161
Spencer AS, Kohn BP, Gleadow AJW, Norman M, Belton DX, Carter T J (2004) The importance of residing in a good neighbourhood: rechecking the rules of the game for apatite (U–Th)/He thermochronology. In: Andressien P (eds) 10th International Fission track Dating Conference, pp. 1–20
Spiegel C, Barry K, Belton D, Berner Z, Gleadow A (2009) Apatite (U-Th-Sm)/He thermochronology of rapidly cooled samples: the effect of He implantation. Earth Planet Sci Lett 285:105–114
Stockli DF (2005) Application of low-temperature thermochronometry to extensional tectonic settings. Rev Mineral Geochem 58:411–448
Tapponnier P, Xu ZQ, Roger F, Meyer B, Arnaud N, Wittlinger G, Yang JS (2001) Oblique stepwise rise and growth of the Tibet Plateau. Science 294:1671–1677
Wang EQ, Burchfiel BC (2000) Late Cenozoic to Holocene deformation in southwestern Sichuan and adjacent Yunnan, China, and its role in formation of the southeastern part of the Tibetan Plateau. GSA Bull 112:413–423
Wang EQ, Yin JY (2009) Cenozoic multi-stage deformation occurred in southwest Sichuan: cause for the dismemberment of the proto-Sichuan Basin. J Northwest Univ Nat Sci Ed 39:359–367
Wang E, Burchfiel BC, Royden LH, Chen L, Chen J, Li W, Chen Z (1998) Late Cenozoic Xianshuihe-Xiaojiang, Red River, and Dali fault systems of southwestern Sichuan and central Yunnan, China: Boulder, Colorado. Geol Soc Am Spec Pap 327:1–108
Wang E, Kirby E, Furlong KP, van Soest M, Xu G, Shi X, Kamp PJ, Hodges KV (2012a) Two-phase growth of high topography in eastern Tibet during the Cenozoic. Nat Geosci 5:640–645
Wang SF, Jiang GG, Xu TD, Tian YT, Zheng DW, Fang XM (2012b) The Jinhe-Qinghe fault: an inactive branch of the Xianshuihe–Xiaojiang fault zone, Eastern Tibet. Tectonophysics 544–545:93–102
Whipp MD, Ehlers AT (2007) Influence of groundwater flow on thermochronometer: derived exhumation rates in the central Nepalese Himalaya. Geology 35:851–854
Wilson CJL, Fowler A (2011) Denudational response to surface uplift in east Tibet: evidence from apatite fission-track thermochronology. GSA Bulletin 123:1966–1987
Wilson CJL, Harrowfield MJ, Reid AJ (2006) Brittle modification of Triassic architecture in eastern Tibet: implications for the construction of the Cenozoic plateau. J Asian Earth Sci 27:341–357
Wolf RA, Farley KA, Kass DM (1998) Modeling of the temperature sensitivity of theapatite (U–Th)/He thermochronometer. Chem Geol 148:105–114
Worley BA, Wilson CJL (1996) Deformation partitioning and foliation reactivation during transpressional orogenesis, and example from the Central Longmen Shan, China. J Struct Geol 18:395–411
Xia ZS (1982) Continental Mesozoic Stratigraphy and Paleontology in Sichuan Basin of China. Geologic Publishing House, Beijing, pp 1–743
Xiang F, Zhu LD, Wang CS, Zhao XX, Chen HD, Yang WG (2007) Quaternary sediment in the Yichang area: implications for the formation of the Three Gorges of the Yangtze River. Geomorphology 85:249–258
Xu GQ, Kamp PJJ (2000) Tectonics and denudation adjacent to the Xianshuihe fault, eastern Tibetan Plateau: Constraints from fission track thermochronology. J Geophys Res 105:19231–19251
Xu YG, Menzies MA, Thirlwall MF, Xie GH (2001) Exotic lithosphere mantle beneath the western Yangtze craton: petrogenetic links to Tibet using highly magnesian ultrapotassic rocks. Geology 29:863–866
Xu L, Rondenay S, van der Hilst R (2007) Structure of the crust beneath the southeastern Tibetan plateau from teleseismic receiver functions. Phys Earth Planet Inter 165:176–193
Xu M, Zhu CQ, Tian YT, Rao S, Hu SB (2011) Borehole temperature logging and characteristics of subsurface temperature in the Sichuan basin. Chin J Geophys 54:1052–1060
Zhang YX, Luo ZN, Yang CX (1990) Panxi Rift and its geodynamics. Geol. Publishing House, Beijing, pp 1–318
Zhang YQ, Chen W, Yang N (2004a) $^{40}Ar/^{39}Ar$ dating of shear deformation of the Xianshuihe fault zone in west Sichuan and its tectonic significance. Sci China Ser D Earth Sci 47:794–803
Zhang PZ, Shen ZK, Wang M, Gan WJ, Bürgmann R, Molnar P, Wang Q, Niu ZJ, Sun JZ, Wu JC, Sun HR, You XZ (2004b) Continuous deformation of the Tibetan Plateau from global positioning system data. Geology 32:809–812
Zhang PZ, Wen XZ, Shen ZK, Chen JH (2010) Oblique, high-angle, listric-reverse faulting and associated development of strain: The Wenchuan earthquake of May 12, 2008, Sichuan, China. Ann Rev Earth Planet Sci 38:353–382
Zhao XT, Hu DG, Zhang YS (2008) Genesis and age of the gravels underlying the Xigeda Formation of Panzhihua Sichuan, China, and valley development of the Ancient Jinsha River. Acta Geosci Sin 29:1–12
Zheng JP, Griffin WL, O'Reilly SY, Zhang M, Pearson N, Pan YM (2006) Widespread Archean basement beneath the Yangtze craton. Geology 34:417–420